

# The Assembly History of Field Spheroidals: Evolution of Mass-to-light Ratios and Signatures of Recent Star Formation

Tommaso Treu<sup>1,2,3</sup>, Richard S. Ellis<sup>3</sup>, Ting Xi Liao<sup>3</sup>, Pieter G. van Dokkum<sup>4,3</sup>, Paolo Tozzi<sup>5</sup>, Alison Coil<sup>5</sup>, Jeffrey Newman<sup>6,2</sup>, Michael C. Cooper<sup>6</sup>, Marc Davis<sup>6</sup>

## ABSTRACT

We present a comprehensive catalog of high signal-to-noise spectra obtained with the DEIMOS spectrograph on the Keck II telescope for a sample of  $F850LP < 22.43$  (AB) field spheroidal (E+S0s; 163) and bulge dominated disk (61) galaxies in the redshift range  $0.2 < z < 1.2$ , selected on the basis of visual morphology from the northern field of the Great Observatories Origins Deep Survey (GOODS-N). We discuss sample selection, photometric properties and spectral reduction. We derive scale-lengths, surface brightnesses and photometric inhomogeneities from the ACS data, and redshifts, stellar velocity dispersions, [O II] and H $\delta$  equivalent widths from the Keck spectroscopy. Using the published 2Ms Chandra X-ray catalog we identify active galactic nuclei to clarify the origin of emission lines seen in the Keck spectra. Only 2/13 [O II] emitting early-type galaxies are identified as secure AGN on the basis of their X-ray emission. Contrary to earlier suggestions, we find that most spheroidals containing ‘blue cores’ are not associated with non-thermal nuclear activity. We examine

---

<sup>0</sup>Using data obtained with the Hubble Space Telescope operated by AURA for NASA and the W.M. Keck Observatory on Mauna Kea, Hawaii. The W.M. Keck Observatory is operated as a scientific partnership among the California Institute of Technology, the University of California and NASA and was made possible by the generous financial support of the W.M. Keck Foundation.

<sup>1</sup>Department of Physics and Astronomy, University of California at Los Angeles, Los Angeles, CA 90095; ttreu@astro.ucla.edu

<sup>2</sup>Hubble Fellow

<sup>3</sup>Caltech, Astronomy, 105-24, Pasadena, CA 91125, USA

<sup>4</sup>Department of Astronomy, Yale University, New Haven, CT 06520

<sup>5</sup>INAF-Osservatorio Astronomico di Trieste via G.B. Tiepolo 11, 34131 Trieste - Italy

<sup>6</sup>Department of Astronomy, UC Berkeley, CA 94720

the zero point, tilt and scatter of the Fundamental Plane (FP) as a function of redshift and morphological properties, carefully accounting for luminosity-dependent biases via Montecarlo simulations. The evolution of the overall FP can be represented by a mean change in effective mass-to-light ratio given by  $\langle d \log(M/L_B)/dz \rangle = -0.72^{+0.07}_{-0.05} \pm 0.04$ . However, this evolution depends significantly on the dynamical mass, being slower for larger masses as reported in a previous letter. In addition, we separately show the intrinsic scatter of the FP increases with redshift as  $d(\text{rms}(M/L_B))/dz = 0.040 \pm 0.015$ . Although these trends are consistent with single burst populations which formed at  $z_f > 2$  for high mass spheroidals and  $z_f \sim 1.2$  for lower mass systems, a more realistic picture is that most of the stellar mass formed in all systems at  $z > 2$  with subsequent activity continuing to lower redshifts ( $z < 1.2$ ). The fraction of stellar mass formed at recent times depend strongly on galactic mass, ranging from  $< 1\%$  for masses above  $10^{11.5} M_\odot$  to 20-40% below  $10^{11} M_\odot$ . Independent support for recent activity is provided by spectroscopic ([O II] emission, H $\delta$ ) and photometric (blue cores and broad-band colors) diagnostics. Via the analysis of a large sample with many independent diagnostics, we are able to reconcile previously disparate interpretations of the assembly history of field spheroidals. We discuss the implications of this measurement for the determination of the evolution of the number density of E+S0s galaxies, suggesting number density evolution of the morphologically selected population has occurred since  $z \sim 1.2$ .

*Subject headings:* cosmology: observations, galaxies: formation, galaxies: evolution, morphologies

## 1. Introduction

The assembly history of field spheroidal galaxies (defined here to include both ellipticals and lenticulars, in short E+S0s) remains an important issue in galaxy formation and particularly in the interface between theory and observation (see Treu 2004, McCarthy 2004 for recent reviews). The overall assembly rate of stellar mass has been constrained both by measures of the cosmic star formation history (Madau et al. 1996, Blain et al. 1999, Steidel et al. 1999, Bunker et al. 2004) and, directly, via photometric estimates of the stellar mass density as a function of redshift (Brinchmann & Ellis 2000, Cohen 2001, Papovich et al. 2001, Rudnick et al. 2003; Fontana et al. 2004). However, such global constraints integrate over important details relating to the formation history of individual morphological types.

A key prediction of current semi-analytical models based on the cold dark matter

paradigm (e.g. Kauffmann 1996, Baugh et al. 1998, Somerville & Primack 1999) is the late assembly of massive spheroids from smaller fragments with significant consequences for the abundance and mass distribution of systems at  $z \simeq 1-2$ . Although the actual rate of assembly is sensitive to details of the algorithms used in the semi-analytical codes (see comparisons in Benson et al. 2003), the observational data has provided only mixed support for the evolution expected.

The simplest evolutionary test is based on measuring the density of spheroids at various redshifts. Brinchmann & Ellis (2000), and more recently Bundy, Ellis & Conselice (2005), found only a modest decline in the *stellar mass density* to  $z \simeq 1$  using morphologically-defined samples (see also Im et al. 2002, Cross et al. 2004). These results appear to contrast with the claim by Bell et al. (2003), based on color-selected samples, that the *luminosity density* associated with red galaxies is fairly constant to  $z \simeq 1$  suggesting a marked drop in the volume density of such objects. The utility of these tests depends sensitively on corrections for incompleteness and cosmic variance.

An independent approach involves estimating the ongoing mass accretion rate for spheroidals, either via the presence of photometric abnormalities such as ‘blue cores’ (Menanteau et al. 2001a,b, 2004, 2005), spectroscopic signatures of recent activity (Trager et al. 2000; Treu et al. 2002; van Dokkum & Ellis 2003) or deviations from passive trends predicted in the evolution of the Fundamental Plane (Djorgovski & Davis 1987, Dressler et al. 1987; hereafter FP; Treu et al. 1999, 2001b, 2002; van Dokkum & Ellis 2003; Gebhardt et al. 2003; van de Wel et al. 2004; Treu & Koopmans 2004; see also Kochanek et al. 2000; Rusin et al. 2003a; van de Ven et al. 2003; Rusin & Kochanek 2005). The degree to which the population is homogeneous in its passive evolution provides a very sensitive measure of the rate at which spheroidals may still be forming. Both tests are valuable but progress on the latter has, until now, been hindered by the small size of the spectroscopic samples available.

This paper is motivated by extending the early work begun in this area via a comprehensive analysis of high quality Keck spectroscopy for 224 morphologically-selected spheroidals and bulge-dominated galaxies in the northern field of the Great Observatories Origins Deep Survey (GOODS). Associated with the Advance Camera for Surveys (ACS) and spectroscopic data discussed here, is *K*-band photometry from which stellar masses and optical-infrared colors have also been derived elsewhere (Bundy, Ellis & Conselice, 2005).

An overview of one of the main results of this observational program has already been presented in Treu et al. (2005; hereafter T05), where we discuss the evolution of dynamical mass-to-light ratios as a function of mass and environmental density in the context of hierarchical models of galaxy formation. We find that mass-to-light ratios – and hence luminosity weighted stellar ages – depend sensitively on the dynamical mass. The most massive galaxies

have evolved passively at least since  $z \sim 1.2$  while less massive systems show strong evidence of recent star formation activity, consistent with a “downsizing” scenario (Cowie et al. 1996). Within the range of environments covered by the GOODS-N field, no dependency is seen between this recent activity and the local galaxy density - contrary to the expectations of hierarchical models of galaxy formation (Diaferio et al. 2001; de Lucia et al. 2004).

In this paper, we considerably extend and quantify the arguments presented in T05 in the context of a unifying hypothesis of the mass assembly history of spheroidals of various masses. We describe in detail our HST and Keck spectroscopic data and present the associated catalogs. We derive the evolution of mass-to-light ratios based on analysis of the Fundamental Plane, taking into account selection effects and correlating deviations from the overall trend with morphological substructures.

A plan follows. In §2 we introduce the GOODS-ACS multicolor imaging dataset, the construction of a photometric catalog and the procedure whereby which morphological types were assigned to all galaxies brighter than  $F850LP < 22.5$  (AB; hereafter  $z_9$ ). Surface photometry and scale-lengths are fit to the sample of spheroidals and morphological substructures identified via pixel-by-pixel color imaging (c.f. Menanteau et al. 2001). §3 presents the Keck spectroscopy and its reduction and the techniques used to measure stellar velocity dispersions. A complete catalog of the spectroscopic and photometric data is presented. §4 describes the correlation of our catalog with the 2Ms X-ray catalog of the Chandra Deep Field North (Alexander et al. 2003; Barger et al. 2003) to identify nuclear activity. In §5 we analyze the zero point, tilt, and scatter on the fundamental plane as a function of redshift, and we use spectral and photometric diagnostics to provide independent evidence for recent star formation. §6 summarizes our findings and discusses our results in the context of formation scenarios for spheroidals.

We assume throughout a cosmological model with  $\Omega_M = 0.3$ ,  $\Omega_\Lambda = 0.7$  and  $H_0 = 65$  km s<sup>-1</sup> Mpc<sup>-1</sup>. All magnitudes are in the AB system (Oke 1974), unless otherwise noted.

## 2. Imaging

Imaging data are taken from the public GOODS survey (Giavalisco et al. 2004). Initial sample selection and planning of spectroscopic observations were performed before the completion of the survey and are based on the v0.5 release of epoch 1 (as described in 2.1). After completion of the GOODS-N survey and the release of the combined v1.0 dataset, the photometric analysis was repeated using the newly processed and deeper images as described in this section.

## 2.1. Photometric catalog

In preparation for our spectroscopic observations in April 2003, a first catalog was produced by running SExtractor (Bertin & Arnouts 1996) on the v0.5 release of epoch 1 of the GOODS images. A  $z_9$  selected catalog was constructed including all objects brighter than  $\text{MAG\_AUTO } z_{9,v0.5} < 22.5$ . We will refer to this catalog as the v0.5-zcatalog. After the release of the combined GOODS images (release v1.0) a further catalog was constructed using the same procedure. We will refer to this catalog as the v1.0-zcatalog. The v1.0-zcatalog is available from Bundy, Ellis & Conselice (2005; URL [http://www.astro.caltech.edu/GOODS\\_morphs/](http://www.astro.caltech.edu/GOODS_morphs/)).

Comparisons between the two catalogs provide an estimate of the photometric accuracy. After adjusting for the different zero points (c.f. the GOODS web page), the median difference and semi-interquartile range in  $z_9$  magnitudes between v0.5 and v1.0 are less than 0.01 and 0.03 mags respectively. Since these are negligible with respect to other sources of errors throughout the paper, our catalog is effectively magnitude selected in v1.0 as well. Accounting for the different zero points, the selection limit corresponds to  $z_{9,v1.0} < 22.43$ . Throughout the rest of the paper, all photometry is based on the v1.0 data and zero points. Absolute magnitudes can be obtained from apparent magnitudes and colors using the transformations described in Appendix A.

## 2.2. ACS Morphologies

In view of the spectroscopic run scheduled in March 2003, an initial morphological classification was undertaken by one of us (RSE) by visual inspection of the v0.5 epoch 1  $z_9$ -band images. The  $z_9$  images were chosen to provide the closest match to optical rest frame at a redshift  $z \sim 1$ , minimizing the so-called morphological  $k$ -correction. Morphologies (hereafter T) were assigned according to the Medium Deep Survey scheme introduced by Abraham et al. (1996a; see also Treu et al. 2003): T=-2=star, -1=compact, 0=E, 1=E/S0, 2=S0, 3=Sa+b, 4=S, 5=Sc+d, 6=Irr, 7=Unclass, 8=Merger, 9=Fault. When the deeper v1.0 data release became available, a blind re-classification was also performed. Throughout the rest of the paper (unless otherwise specified) and in the published catalog, all morphological types are based on the deeper v1.0 data. Early-type and Sa+b galaxies in the final spectroscopic sample are shown in Figures 2 and 3.

Comparison between the two morphological catalogs provides a check on the internal consistency of the classification and on its sensitivity to signal-to-noise (Figure 1). Considering the entire sample, the agreement is very good, with a median offset of 0, a mean offset of -0.1 and a standard deviation of 1.3 (in the 12 point T scheme described above). However,

for the class of spheroidal objects with  $T=0,1,2$  in the v0.5 catalog, the mean offset increases to 0.4 (median=0, standard deviation 1.2). The differences arise because of the improvement in signal-to-noise in the v1.0 images which reveal, when present, the characteristic low surface brightness features of spiral disks. Thus objects classed as spheroidals in the v0.5 catalog (which formed the basis of our spectroscopic sample) include some systems which later turned out to be bulge-dominated spirals, as described quantitatively in Section 3.1. Of course, by including these outliers in our sample, we have a valuable measure of the uncertainties associated with defining our morphological boundaries.

Although we include our morphological classifications in the large catalog discussed by Bundy, Ellis & Conselice (2005), it is important to examine the extent to which classification uncertainties permitted in large statistical analyses might influence the results of this, more focused, study of a relatively small number of spheroidals. A particular concern is the likelihood of contamination by the more numerous bulge-dominated spirals.

We can estimate the probability of spiral contamination as follows. At the magnitude limit of the survey, the rms scatter  $\text{rms}_{\text{tot}}$  in classification between the v0.5 and v1.0 catalogs is 1.3 types. Assuming that uncertainties scale as the square root of the exposure time, we obtain  $\text{rms}_{\text{tot}} = \sqrt{\text{rms}_{1.0}^2 + \text{rms}_{0.5}^2} = \sqrt{\text{rms}_{1.0}^2 + 5\text{rms}_{1.0}^2}$ , since the v1.0 images represent 5 times the integration of the v0.5 images. This would appear to be a conservative assumption, since the v1.0 images also have improved sampling, defect removal and relative alignment. Thus, we expect  $\text{rms}_{1.0} = \text{rms}_{0.5} / \sqrt{6} \sim 0.5$  implying that  $\sim 1/6$  of the Sa+b sample might be misclassified as S0s. As Sa+bs are twice as numerous as S0s overall, we estimate that  $\sim 1/3$  of the S0s could be misclassified Sa+bs, i.e. approximately 20.

To identify possible misclassified Sa+bs, residuals from the  $r^{1/4}$  fitting (faint analogs of the ones shown in Figure 4) were visually inspected by two of us (RSE,TT) for disk asymmetries and spiral features. To be conservative, all edge-on S0s, where inclination could be hiding spiral features, were also flagged. With these criteria, we identified 23 possible Sa+b contaminants (ID 199, 312, 369, 400, 402, 424, 505, 63, 655, 786, 811, 870, 872, 895, 996, 1286, 1441, 1463, 1485, 1491, 1577, 1685, 1764). The technique is surprisingly effective in locating faint spiral features but we use this flagging only to illustrate the effect of possible contamination rather than to refine the published morphological catalog. We also identified 7 galaxies with prominent dust lanes or asymmetries (ID 312, 377, 460, 879, 1354, 1477, 1764) where the dust and asymmetries could bias photometric and spectroscopic parameters used in our analysis. In Section 5.3 we will test the robustness of our analysis with respect by these possible biases by comparing results obtained with and without these two subsamples.

### 2.3. Surface photometry

Surface photometry of all early-type galaxies and bulge dominated spirals targeted for spectroscopy was performed using the publicly available software GALFIT (Peng et al. 2002). Effective radius ( $R_e$ ) and magnitudes (and hence effective surface brightness  $SB_e$ ) were obtained in all four bands as the best fitting parameters of a  $r^{1/4}$  surface brightness profile, following the standard procedure used to construct the Fundamental Plane (Jørgensen, Franx & Kjaergaard 1992; van Dokkum & Franx 1996; Treu et al. 2001). The fitting procedure requires a point spread function (PSF) to convolve the model before computing the  $\chi^2$ . For each galaxy we adopted the nearest bright non-saturated star in the GOODS-N field as fiducial PSF, thus correctly taking into account the modifications of the PSF due to the GOODS v1.0 reduction procedure. Examples of fits and residuals from a  $r^{1/4}$  profile are shown in Figure 4.

As is commonly known (e.g. Kelson et al. 2000a; Treu et al. 2001a) the particular combination of photometric parameters necessary for constructing the FP:  $FP_{ph} = \log R_e - 0.32SB_e$ , is limited for datasets of good quality such as GOODS by the fitting technique. Tests with fit2D (Treu et al. 2001a) indicate that the  $FP_{ph}$  parameter derived using GALFIT is consistent with those derived in previous studies to a level of 0.02 or better. An additional test can be obtained by comparing our photometry to the one of vDE03, for the 9 objects in common. The effective radii agree extremely well (average difference  $\log R_e = 0.0004$ , rms scatter 0.066), and the photometry is in good agreement ( $F814W - F775 = 0.010$  mag, with rms = 0.34 mag) considering the different filters and instruments (assuming  $F814W = F775W$ ). As a result  $FP_{ph}$  agrees well (average difference 0.019, rms 0.051).

We adopt 0.03 as our best estimate of the systematic uncertainty on the  $FP_{ph}$  due to the fitting technique. Absolute magnitudes can be obtained from apparent magnitudes and colors using the transformations described in Appendix A (c.f. Treu et al. 2001a). Rest frame effective radii are obtained by interpolation from the two nearest filters as described in Treu et al. 2001a.

### 2.4. Internal colors, blue cores and morphological asymmetry

The GOODS images are, like their HDF predecessors, of adequate signal to noise for us to examine the internal homogeneity as a verification of the morphological classifications and as a possible diagnostic of recent activity. Of particular interest, given our large sample with associated spectroscopy are the so-called ‘blue-core’ spheroidals first identified by Menanteau et al. (2001) in the HDF images. In this paper we define a more robust way to uniformly

select such systems at various redshifts and our resulting sample is significantly larger than any hitherto.

Rest frame pixel-by-pixel color maps (B-V) were derived by applying the transformations described in Appendix A, with the aim of identifying internal color peculiarities which might indicate recent starformation activity. The vast majority of early-type galaxies proved to be relatively smooth and homogenous. However 14/163 early-type galaxies with measured redshift show a clear blue core.

Menanteau et al. (2001) already addressed the key issue of whether the blue cores could be artefacts arising from the wavelength dependency of the HST PSF. Although that analysis was conducted on the basis of WFPC-2 images in the Hubble Deep Field and rich clusters, the improved spatial sampling of the ACS makes their arguments tighter in this case. An instrumental origin would imply a much greater frequency of blue cores at a given apparent magnitude and not produce the environmental dependencies discussed by Menanteau et al. or the correlations with independent diagnostics of star formation discussed below.

We chose to define a blue core spheroidal as one where a difference of at least  $\delta(B-V)=0.2$  is seen between the core of the galaxy and the outer parts. As our color selection is made in rest-frame color, this is significantly more useful than the observed  $V - I$  criterion used in previous studies (Menanteau et al. 2001, 2004, 2005). We find a total of 14 blue-core early-type galaxies in GOODS-N and these are sorted by redshift and shown in Figure 5. The nature of these systems is discussed further in Sections 4 and 5.6.

### 3. Keck Spectroscopy

#### 3.1. Sample selection and mask design

The sample for spectroscopic follow-up was selected from the v0.5-zcatalog according to the following criteria:  $z_{9,v0.5} < 22.5$ ,  $-1 \leq T \leq 2$ . Self-consistent astrometry across the field was obtained by matching the ACS catalog to the ground based catalog used by the Team Keck Redshift Survey (TKRS; Wirth et al. 2004). Three sets of masks with their major axis aligned with that of the GOODS-N mosaic were designed (north, center, south). For each pointing a first submask was filled with objects at random from the sample of early-type galaxies using the v0.5 morphologies. A second submask was obtained by replacing objects brighter than  $z_{9,v0.5} = 21.5$  with new objects. The goal of this procedure was to obtain longer exposure times for the faintest objects while maximizing the number of survey objects.

In total, 261 galaxies from the primary spectroscopic sample were included in the six



masks, plus 22  $T=3$  (v0.5) galaxies. Based on the subsequently-determined deeper v1.0 morphologies, the spectroscopic sample 175 early-types, 66 early-spirals ( $T=3$ ), 14 later type galaxies ( $T>4$ ) and 28 stars. This mixing of types is expected because of the increased signal-to-noise in the v1.0 (see section 2.2) images and because the number of objects that can drift out of the sample due to random errors in the classification is much larger than the number of objects that can enter, and because a conservative star/galaxy separation criterion was used in the v0.5 images.

Eighteen slitlets (with a random distribution of morphologies and luminosities) were not milled or could not be extracted because they fell too close to the edges of the masks, so the final tally is comprised of 265 objects. Six objects were observed twice, in different slitlets of different masks, to allow for internal checks. All the galaxies with measured redshifts are shown in Figure 2 and Figure 3.

To ensure that the retrospective v1.0 morphological cut does not bias the properties of our sample we compare in Figure 6 the luminosity and color distribution of the parent sample comprising all early-type galaxies in the GOODS-N field (v1.0, empty histogram) with defined in our spectroscopic sample (v0.5, hatched histogram). The color distributions are very similar with a typical sampling rate between 50 and 70%, showing that our spectroscopic sample is unbiased in color. However, the sampling rate is a declining function of apparent magnitude beyond  $z_9 \sim 21.5$ , as expected, because of our mask-design strategy, the higher surface density and the higher probability of morphological misclassification.

In the following we will consider the early-type galaxies as our primary sample. The early-spiral sample (composed mostly of objects classified as early-type in the v0.5 analysis) will be useful as an ancillary in order to compare with results based on shallower imaging data. A complete discussion of the properties and star formation histories of the bulges will be given elsewhere.

### 3.2. Observations and data reduction

The field was observed using the Deep Imaging and Multi-Object Spectrograph (DEIMOS) at the Keck-II telescope on the nights of April 1 to 5 2003. Conditions were excellent, with clear sky and seeing in the range  $0''.6$ – $0''.8$  throughout the run. The 1200 grating blazed at  $7500\text{\AA}$  was centered at  $8000\text{\AA}$  providing a pixel scale of  $0''.1185 \times 0.33\text{\AA}$ , and a typical wavelength coverage of  $2600\text{\AA}$ . The  $1''.0$  wide slitlets yielded an instrumental resolution of  $\sigma_s \sim 20 - 30\text{ km s}^{-1}$ , as determined from arc lines and sky emission lines. Total exposure times ranged between 14,400 and 38,900 seconds as listed in Table 1.

The data were reduced using the IDL pipeline developed by the DEEP2 collaboration (Davis et al. 2003; Faber et al. 2005, in prep). After extraction, the 1d spectra were assigned a redshift using the software developed by the DEEP2 collaboration (described in Coil et al. 2004). All spectra were examined independently by two of us (TT and TXL) and a quality criterion was assigned ( $q=-1$  stars,  $q=2$  possible,  $q=3$  likely,  $q=4$  certain). In those very few cases where the redshift/quality parameter differed, a simultaneous inspection by the two classifiers was sufficient to reach an agreement.

Redshifts were obtained for all the 265 targeted objects, including 217 from the primary sample, 21 Sa+b galaxies, and 27 that turned out to be stars (v0.5 classification). Based on the superior v1.0 classifications, the sample with redshifts is comprised of 163 early-type galaxies, 61 early-spirals, 23 later type galaxies and 1 star (according reclassified as compact). Comparison with other surveys shows that our redshifts are accurate to  $30 \text{ km s}^{-1}$  or better (c.f. Wirth et al. 2004). An approximate relative flux calibration was obtained using the measured sensitivity curves for DEIMOS. Examples of spectra covering the range of redshifts and luminosities (and hence signal to noise ratio) are given in Figure 7. The redshift distribution of the E+S0 and Sa+b samples is shown in Figure 8.

### 3.3. Internal kinematics

Stellar velocity dispersion were obtained by comparing the extracted spectra with spectra of G-K giants and of the Sun (a high resolution solar spectrum was obtained from the URL [http://bass2000.obspm.fr/solar\\_spect.php](http://bass2000.obspm.fr/solar_spect.php)) as described in detail in Treu et al. (1999; 2001) and in Sand et al. (2004). A brief summary follows.

First, the instrumental resolution was measured by fitting gaussians to well-exposed and unblended sky lines and arc calibration lamps. This corresponds to a velocity dispersion of  $\sigma_s = 30 - 20 \text{ km s}^{-1}$  in the spectral range of interest, and is well described by a second order polynomial in wavelength  $\sigma_s(\lambda)$ . Second, high resolution template stars were redshifted and smoothed to match the resolution of the instrumental setup, and convolved with gaussians in  $\log \lambda$  space to reproduce the kinematic broadening. The best fitting velocity dispersion was found using the pixel fitting code developed by van der Marel (1994). Spectral regions affected by emission lines, Balmer lines, atmospheric A and B band absorption, as well as residual defects were carefully masked out during the fit. Those pixels affected by the strongest sky emission lines and their immediate neighbors were similarly flagged. Each object was fitted independently with each template and using different spectral regions. The G-K giant library extends from  $4000 \text{ \AA}$  redwards, while the solar spectrum extends to the UV atmospheric limit, enabling us to take advantage of near-UV absorption features in the

highest redshift objects (c.f. van Dokkum & Stanford 2003).

Each spectrum and fitting result was carefully inspected by eye by one of us (TT) to identify and correct potential problems (such as insufficient wavelength range or reduction/extraction defects). Two example of spectra with kinematic fits – an intermediate quality spectrum and the highest redshift object with measured velocity dispersion – are shown in Figure 9.

The majority (181/224 of all galaxies; 141/163 spheroidals) of objects yielded a stable velocity dispersion measure ( $\sigma_{\text{ap}}$ ) listed in Table 1. A few objects failed to deliver a reliable velocity dispersion, due to insufficient signal to noise or unfortunate location of the strongest absorption features on persistent sky subtraction residuals. For a handful of objects at low redshift the procedure yielded velocity dispersions below the instrumental resolution  $\sigma_s = 30 \text{ km s}^{-1}$ . These measures were considered insufficiently reliable enough and discarded (although plausibly correct given their faint intrinsic luminosity and the fact that the NaD line is resolved). The success rate as a function of redshift, luminosity, and average signal to noise ratio (per Å, observer frame) is summarized in Figure 10. For simplicity, we report the average signal to noise ratio across the entire spectrum as a measure of the total information, which is approximately given by  $\langle S/N \rangle$  multiplied by the square root of the number of Å, i.e.  $\sqrt{2600}$ . The  $\langle S/N \rangle$  per Å in the rest frame is readily obtained as  $\langle S/N \rangle_{\text{rest}} = \langle S/N \rangle \sqrt{1+z}$ . As other authors (e.g. Jørgensen, Franx & Kjaergaard 1995) often quote values based on smaller wavelength regions, or ones longward of the 4000 Å break, in comparing the limiting  $S/N$  for which dispersions were successfully measured, differences in definition should be borne in mind (see Figure 11).

For the FP analysis, the central velocity dispersions (i.e. within a circular aperture of radius  $r_e/8$ ) was obtained as  $\sigma = 1.10 \pm 0.04 \sigma_{\text{ap}}$  (Treu et al. 2001).

### 3.4. Tests of the Measured Velocity Dispersions

Given the size of our sample, a key issue before the scientific analysis that follows is the reliability of our stellar velocity dispersions. We have approached this via several independent tests which, collectively, demonstrate a high degree of precision has been attained, thanks largely to the long integrations and the excellent quality of the data obtained with the DEIMOS spectrograph.

1. Repeated measures of six objects observed with DEIMOS in different slitlets/configurations (Figure 11) show that our measurements are stable with respect to internal effects such

as varying the wavelength range and the slitlet position in the field of view of the spectrograph.

2. A comparison with the 7 objects in common with van Dokkum & Ellis (2003) examined independently with the LRIS spectrograph shows that both sets are also statistically indistinguishable, with  $\langle \delta\sigma/\sigma \rangle = -0.06$  and an rms scatter of 12 %, consistent with the estimated errors ( $0.12/\sqrt{6} = 0.05$ ).
3. A subsample of spectra were analyzed independently by one of us (PGD) using methods described in van Dokkum & Franx (1996). The internal comparison indicates stellar velocity dispersions that agree to better than 1% on average, with an rms scatter of 12%, indicating that there are no significant systematic uncertainties due to the choice of fitting method.

We conclude that our estimated errors on velocity dispersion (on average less than 10%) are accurate.

### 3.5. Basic Star Formation Diagnostics: [O II] and H $\delta$

Whenever the redshift placed the useful diagnostic features of [O II] 3727 Å and H $\delta$  4101 Å in the observed spectral region, we measured their equivalent widths using an IDL procedure. The band definitions of Fisher et al. (1998; [O II]) and Trager et al. (1998; H $\delta_A$ ) were used. The noise properties of the spectra were taken into account so as to maximize the signal-to-noise ratio. Observed frame equivalent widths in Å are listed in Table 1 In the following analysis we will always refer to rest frame equivalent widths in Å.

## 4. X-ray properties

To obtain a complementary source of information on nuclear activity and star formation in our sample of spheroidals (and in particular on the blue cores) we cross correlated our redshift catalog with the published X-ray 503 sources catalog of the Chandra Deep Field North (Alexander et al. 2003; Barger et al. 2003), finding 42 sources with X-ray counterparts (26 E+S0s; 13 Sa+bs; 3 Ss). All the 42 sources have redshifts published in Barger et al. (2003), in agreement with our determinations.

From the soft and hard fluxes measured in Barger et al. (2003), we derive the rest frame soft (0.5–2 keV) and hard (2–8 keV) emitted luminosities applying a  $k$ -correction for

a spectrum with photon index  $\Gamma = 2$ . A spectral slope of  $\Gamma = 2$  is appropriate for X-ray emission from prompt star formation. Since the majority of the 42 X-ray counterparts of our spheroidal galaxies have emitted luminosities in the range typical of star forming galaxies ( $L_{0.5-2} \leq 10^{42}$  erg s $^{-1}$ , see Ranalli et al. 2003), we concluded that  $\Gamma = 2$  is a good approximation of the required  $k$ -correction. Adopting a different  $k$ -correction has a negligible impact on our results, as described in the next paragraph.

For simplicity, we will classify our objects as AGN-dominated if the X-ray luminosity (soft or hard) is above  $10^{42}$  erg s $^{-1}$ , and as star formation dominated or low luminosity AGN (LLAGN) if it is not in the previous category and the X-ray luminosity is above  $10^{40}$  erg s $^{-1}$  (in the following we will label these two groups as XAGN and XSF/LLAGN; motivations for these working definitions is given in Appendix B). With these definitions, 17 sources (9 E+S0s) are XAGNs while 21 (16 E+S0s) are XSF/LLAGNs. Adopting different slopes for the  $k$ -correction, e.g.  $\Gamma \simeq 1.4$  typical of the average spectrum of absorbed and unabsorbed AGN that dominate the population in the faint flux regime (as in the CFDN), would only adjust these numbers in a minor way to 16 and 20 galaxies respectively in the XAGN and XSF-LLAGN categories. The same classification is obtained by adopting the spectral slope evaluated for each source from the X-ray hardness ratio (see Alexander et al. 2003). Interestingly, only 2 of the 14 blue cores E+S0s are classified as XAGN (ID=1323,872 Figure 5), while 1 is classified as XSF-LLAGN (ID=1362), showing that most blue cores are not due to a central AGN.

For the X-ray sources classified as XSF/LLAGN we can obtain an upper limit to the star formation rate using the conversion  $\dot{M} = 2.2 \times 10^{-40} L_{0.5-2keV} \text{ M}_{\odot} \text{ yr}^{-1}$  (Ranalli, Comastri & Setti 2003). The upper limits are in the range 1-100  $\text{M}_{\odot} \text{ yr}^{-1}$  with an average (median) value of  $38 \pm 30 \text{ M}_{\odot} \text{ yr}^{-1}$  ( $28 \pm 23 \text{ M}_{\odot} \text{ yr}^{-1}$ ). We would like to emphasize that in many of these cases, these upper limits will be well above the actual star formation rate, because of the LLAGN contribution and/or emission from X-ray halos and LMXB. This is confirmed also by the optical spectra which do not show the dramatic features that would be expected for star formation rates of order  $\sim 20 \text{ M}_{\odot} \text{ yr}^{-1}$ . In order to disentangle more accurately the various contributions – especially the soft extended halos from the typically hard and point-like AGN – a detailed analysis of the spectrum and the spatial distribution of the X-ray emission will be necessary. This goes beyond the scope of the present paper and is left for future work.

## 5. Results

In this section we use our measurements to study the evolution of the stellar populations of early-type galaxies, using the FP as a primary diagnostic tool. In § 5.1 we derive the formalism to interpret the evolution of slopes, intercept and scatter of the FP in terms of (mass dependent) evolution of the effective mass-to-light ratio. In the following sections, § 5.2 and § 5.3, we will use the FP to study, first qualitatively and then quantitatively, the evolution of the mass-to-light ratio of spheroidal galaxies, showing that both the slope and scatter of the FP change with redshift. We will interpret these results in terms of the evolution of the stellar populations. In § 5.5 we will compare our results with the existing literature, showing that previously considered discrepant results can be reconciled if the proper selection effects and uncertainties are taken into account. Finally, in § 5.6, we will examine the relationship between the evolution of the mass-to-light ratio and other stellar population diagnostics, providing independent evidence for recent starformation.

### 5.1. The Fundamental Plane as a diagnostic of stellar populations

The Fundamental Plane is defined as

$$\log R_e = \alpha \log \sigma + \beta \text{SB}_e + \gamma, \quad (1)$$

( $\sigma$  in  $\text{km s}^{-1}$ ,  $R_e$  in kpc,  $\text{SB}_e$  in  $\text{mag arcsec}^{-2}$ ). For this study we will adopt as the local relationship the FP of the Coma cluster ( $\alpha = 1.25$ ,  $\beta = 0.32$ ,  $\gamma = -8.970$ , in B(AB) for  $H_0 = 65 \text{km s}^{-1} \text{Mpc}^{-1}$ ; Jørgensen, Franx & Kjaergaard 1996, hereafter JFK96). We use Coma as the local reference for both cluster and field to minimize systematic uncertainties related to filter transformations, distance determination, and selection effects; see discussion in Treu et al. (2001b). However, the effect of the systematic uncertainty in the local intercept will be discussed and quantified in the analysis. We will also adopt 0.08 in  $\log R_e$  as the intrinsic scatter of the local relationship, consistent with cluster and field estimates (JFK96, Bernardi et al. 2003).

A simple physical interpretation of the FP (Faber et al. 1987) can be given by defining an effective mass,

$$M \equiv \frac{5\sigma^2 R_e}{G}, \quad (2)$$

(c.f. Bender, Burstein & Faber 1992), and by defining the luminosity in the usual way

$$-2.5 \log L \equiv \text{SB}_e - 5 \log R_e - 2.5 \log 2\pi, \quad (3)$$

and by considering an effective mass-luminosity relation of the form (also known as the “tilt” of the FP; e.g., Ciotti, Lanzoni & Renzini 1996; Lanzoni et al. 2004)

$$L \propto M^\eta. \quad (4)$$

These assumptions lead directly to the FP relation given above, provided

$$\alpha - 10\beta + 2 = 0, \quad (5)$$

(van Albada, Bertin & Stiavelli 1995), with  $\eta = 0.2\alpha/\beta$ , which is very closed to the observed value. When converted in solar units and in the form of equation 4, reads:

$$\log M/L_B = 0.25 \log M - 1.934. \quad (6)$$

In this framework, variations of the slopes  $\alpha$ ,  $\beta$  and the intercept  $\gamma$  as a function of redshift are easily interpreted as general trends in luminosity evolution of the stellar populations. If  $\sigma$  and  $R_e$  do not evolve with redshift, for an individual galaxy (labeled by the superscript  $i$ )

$$\gamma^i \equiv \log R_e^i - \alpha \log \sigma^i - \beta \text{SB}_e^i, \quad (7)$$

the offset with respect to the prediction of the FP ( $\Delta\gamma^i \equiv \gamma^i - \gamma$ ) is related to the offset of the  $M/L$  by

$$\Delta \log \left( \frac{M}{L} \right)^i = -\frac{\Delta\gamma^i}{2.5\beta}, \quad (8)$$

which can be used to measure the average evolution and/or scatter of  $M/L$  at given  $M$  (Note that equations 7 and 8 are independent of the evolution of slopes and that this relation does not require the FP to be of the form in Equation 6.). Therefore, the tightness of the FP (JFK96; Bernardi et al. 2003) constrains the homogeneity of the stellar populations of early-type galaxies (similarly to the small scatter of the color-magnitude relation, Bower, Lucey & Ellis 1992). An evolution with redshifts of the slopes of FP can be interpreted in terms of a mass dependent evolution of  $M/L$ . For a FP of the form in Equation 6 the evolutionary rate depends only on effective mass:

$$\frac{d \log(M/L)}{dz} = \frac{1}{2.5} \left[ \frac{d\alpha}{dz} \frac{\gamma - \log M - \log G + \log 5}{10\beta} - \frac{d\gamma}{dz} \right]. \quad (9)$$

In the following, we will often compare the evolution of the FP for field early-type galaxies to that found for cluster E+S0s. For this purpose, we will adopt as our fiducial evolution for E+S0 in massive clusters

$$d \log(M/L_B)/dz = -0.46 \pm 0.04 \quad (10)$$

(van Dokkum & Stanford 2003; see also van Dokkum et al. 1998, who find  $-0.49 \pm 0.05$ ). We also define a parameter that measures the differential evolution between the mass to light ratio of a field E+S0 and that expected for the fiducial cluster E+S0:

$$\delta\Delta\log(M/L_B) = \Delta\log(M/L_B) + 0.46z. \quad (11)$$

## 5.2. Evolution of the FP: qualitative results

The location of the E/S0 (pentagons) and Sa+b (stars) galaxies in the FP-space is shown in the five panels of Figure 13, each panel showing galaxies in a different redshift bin. The local relationship measured in the Coma cluster (JFK96) is shown as a solid line for reference (see Section 5.1 for discussion). The early-type galaxies define a relatively narrow FP in each redshift bin (note that the finite size of the bin introduces some artificial scatter), while the scatter is larger for Sa+b galaxies. As illustrated in T05, galaxies move away from the local relationship as redshift increases, becoming brighter at fixed effective radius and velocity dispersion.

The offset from the local relationship can be converted into a change in effective mass-to-light ratio using Eqn 7 and 8. The change for each individual galaxy as a function of redshift is shown in Figure 14. Evolutionary tracks for a simple (single-burst) stellar population<sup>1</sup> formed at  $z_f = 1, 2, 5$  are also shown for comparison. It is clear that even the genuine E+S0 population spans a wide range in  $\Delta\gamma_i$ , covering the entire range predicted by these simple models. We show these models only for illustration at this point; such formation epochs would refer approximately to the luminosity weighted age of the stellar population. Even a modest fraction of younger stars would have a significant influence on the mass-to-light ratio (Trager et al. 2000; Treu et al. 2001b).

As discussed in T05, the observed change in the slope in Figure 13 and increased scatter in Figure 14 with respect to local samples, are the result of mass-dependent trends, combined with selection effects and increased intrinsic scatter of the FP. This is illustrated in Figure 14 by plotting the offset from the local FP as a function of galaxy mass. The most massive galaxies ( $M > 10^{11.5} M_\odot$ ) have relatively high mass-to-light ratios, minimal scatter and follow the passively-evolving track with a high formation epoch fairly closely. As less massive galaxies are included, the scatter and the average offset from the local relation increase. This possible trend was already tentatively seen in previous studies (Treu et al. 2002; van

---

<sup>1</sup>Unless otherwise stated all evolutionary models are computed using Bruzual & Charlot 1996 stellar population synthesis models GISSEL96, Salpeter IMF, solar metallicity and Kurucz atmosphere models.



der Wel et al. 2004; see Pahre 1998, Kelson et al. 2000c, Wuyts et al. 2004, Moran et al. 2004 for similar results in the cluster context), but only with our large sample does it seem conclusive (T05). In the next section we will obtain quantitative limits on the evolution of the mass-to-light ratio and its scatter as function of mass and redshift taking due account of selection biases.

### 5.3. Evolution of the FP: quantitative results

As we have seen in the previous section, the evolution of the FP depends on galaxy mass, therefore we need to allow the FP slopes to vary with redshift. In addition, since at face value it appears that the intrinsic scatter around the FP increases with redshift, the question of possible evolution in the intrinsic scatter is of great interest. As shown in Treu et al. (2001b; 2002) the evolution of intercept, slope and scatter are interconnected and deeply dependent on selection effects. The larger the intrinsic scatter, the larger the Malmquist-like bias on the evolution of the mass-to-light ratio, and therefore the larger the correction necessary to recover the “unbiased” evolutionary trend.

The bias due to luminosity selection is illustrated in Figure 15 where we show the location of the early-type galaxies in a different projection of the FP: the  $M - M/L$  plane (analogous to the  $\kappa$  space introduced by Bender, Burstein & Faber 1992). The dotted line represents the local relationship, while as in Figure 13 the pentagons represent the early-type galaxies. Hatched regions represent those excluded by our magnitude limit. As expected, objects with low mass and high mass to light-ratio are excluded *a priori* from the sample. Only the two lowest redshift bins probe deep enough to sample the entire FP. At  $z \sim 0.5$  and above, selection effects begin to dominate the low mass trends. Although we now embark on a rigorous modeling of the biases, we can already infer from the existence of galaxies brighter than the selection limit that the intrinsic scatter probably increases with redshift and therefore that the smaller mass galaxies have a diverse star formation history.

We note, in passing, that it is not sufficient to deduce evolutionary trends by considering the high-mass objects only (e.g. van der Wel et al. 2004), since the uncertainties on  $M/L$  and  $M$  are correlated. Selecting objects above a certain mass would introduce an additional bias, leading in general to an overestimate of the  $M/L$  and hence an underestimate of the evolution of this subset of the population. In short, there is no way to avoid a proper modeling of the observables.

### 5.3.1. A Bayesian-Montecarlo approach

Selection effects can be properly taken into account by using the Bayesian-Montecarlo method introduced by Treu (2001) and Treu et al. (2001, 2002). Briefly, the method uses a Montecarlo algorithm to compute the likelihood of obtaining the observed surface brightnesses for fixed velocity dispersion and effective radius, given the uncertainties and sample selection properties as a function of the FP coefficients and scatter. The likelihood is then combined with a prior using Bayes Theorem (1768) to recover the posterior probability for each parameter. The likelihood is generally non-zero over a small region of the possible parameter space and therefore the precise choice of the prior is not critical, assuming that is chosen to be regular enough. In the following, we adopt a uniform prior (see Treu et al. 2001 for a discussion). All results presented in this refer only to the spectroscopic sample of E+S0 galaxies, that is spirals are excluded.

In this section we will derive formal limits on the evolution of the coefficients of the FP using increasingly complicated models. As a first step, we consider a simplified model where only the FP intercept  $\gamma$  and scatter are allowed to vary linearly with redshift, and we thus seek limits on the derivative. This is the traditional approach taken by most studies and therefore it is useful for comparison with previous work. This procedure gives an estimate of the average mass to light ratio evolution of the sample and an upper limit to the evolution of the scatter. By construction the scatter for fixed slopes is always larger than the scatter around the best fitting slopes. The posterior probability contours for our sample in this case are shown in Figure 16.

As expected the constraints on the two quantities are correlated in the sense that less evolution in the mass to light ratio is required for a population with larger scatter. The hypothesis that the FP evolves with a fixed slope and constant scatter is rejected by our dataset. The best estimate and 68% limits (obtained as described in T01) are  $d\gamma/dz = 0.58^{+0.04}_{-0.06}$  and  $d\sigma_\gamma/dz = 0.18^{+0.03}_{-0.04}$  corresponding to  $< d\log(M/L_B)/dz > = -0.72^{+0.07}_{-0.05}$  and  $d\sigma_{\log M/L}/dz < 0.26$ . As shown in Figure 16, the average evolution of the mass-to-light ratio for our sample of field E+S0s is significantly faster than that of cluster E+S0s.

To verify that our results are not influenced by the inclusion of galaxies with dust-lanes or possible early-type spirals, we re-ran our Montecarlo simulations excluding the objects flagged in Section 2.2. Excluding the dusty/peculiar objects (5 with measured velocity dispersion), changes the posterior probability in a negligible way. Excluding the possible Sa+b galaxies (22 with measured velocity dispersion) changes the above limits to  $< d\log(M/L_B)/dz > = -0.75^{+0.10}_{-0.05}$  and  $d\sigma_{\log M/L}/dz < 0.28$ , i.e. much less than the uncertainties (see Figure 16). We conclude that uncertainties in the morphological classification, although likely at the level discussed, do not affect our results.

In addition, we compute the effects of systematic uncertainties on the local intercept. For simplicity, we will express variations in the local intercept as variations in surface brightness  $SB_e$  at a fixed velocity dispersion and effective radius (c.f. Bernardi et al. 2005). Since the evolution depends linearly on the local intercept, there is a simple linear relation between uncertainties, i.e.  $\delta d\log(M/L_B)/dz = -0.57 \delta SB_e$ , where the coefficient is a weighted average of individual redshifts and offsets (the coefficient has been verified numerically by repeating the Montecarlo simulations after varying the local intercept). The environmental dependence of the intercept in the local universe is very small and hard to quantify because of selection effects, filters and parameters definitions. As a conservative approach, we will adopt the maximum environmental difference observed in the Sloan data (Bernardi et al. 2005), corresponding to  $\delta SB_e = 0.075$  mags, i.e. a systematic error on the evolutionary rate of  $\pm 0.04$ .

Next, we consider a more realistic evolutionary scenario: namely evolution of the slopes  $\alpha$  and  $\beta$ , and hence mass dependent evolution (Equation 9). In implementing this model, we assume that the FP can be described with a simple power law relation between  $M$  and  $M/L$  at any redshift, i.e.  $\alpha(z) - 10\beta(z) + 2 = 0$ . We will also assume that evolution of the coefficients and slopes can be described by a linear relation, e.g.  $\alpha(z) = \alpha(0) + d\alpha/dz|_0 z$ . Thus our model has three free parameters,  $d\alpha/dz|_0$ ,  $d\gamma/dz|_0$  and  $d\sigma_\gamma/dz|_0$ . For simplicity, we will drop the index 0, assuming all derivatives are computed at  $z = 0$ .

Posterior probability contours (68% and 95%) for  $d\alpha/dz$  and  $d\gamma/dz$ , marginalized over  $d\sigma_\gamma/dz$ , are shown in Figure 17. Constant slopes are clearly rejected, demonstrating unambiguously that the tilt of the FP evolves with redshift. This result is translated in terms of effective mass to light and mass in Figure 18 using Eqn 9. The evolution of the mass to light ratio depends strongly on mass: the most massive galaxies evolving similarly to massive cluster galaxies (i.e.  $d\log(M/L_B)/dz = -0.46$ ), while evolution is faster for smaller masses. This is the *downsizing* trend discussed in T05.

As a final step, we derive the posterior probability distribution function for the evolution of the intrinsic scatter of the FP  $d\sigma_\gamma/dz$  – marginalized over  $d\alpha/dz$  and  $d\gamma/dz$  – shown in Figure 19. The peak value of the probability distribution of function and the 68% contours are  $d\sigma_\gamma/dz = 0.032 \pm 0.012$ , corresponding to  $d\text{rms}(\log M/L_B)/dz = 0.040 \pm 0.015$ . Note this measurement of the scatter is much smaller than the scatter at fixed slopes (Figure 16), showing that part of the visual impression of the scatter when the evolution is plotted as in Figure 14 is dominated by the change in the slope. This proves that the scatter in the FP, and therefore the scatter in stellar population properties, increases with redshift, as expected for example if the scatter is due to a spread in stellar ages.

#### 5.4. Implications for the star formation history of E+S0 galaxies

In this section we proceed to interpret our findings on the evolution of the FP in terms of star formation and assembly history of E+S0 galaxies. Since only objects morphologically identified as E+S0 are included in our sample, what we describe is the effective star formation history of the existing population at any given redshift. If there was significant morphological evolution (“progenitor bias”, as discussed by van Dokkum & Franx 2001 for cluster early-type galaxies), the average star formation activity of the parent population would be more delayed.

First, we will use single burst stellar population models showing that they imply very low redshift of formations for the population with effective mass below  $10^{11} M_{\odot}$ , inconsistent with independent star formation diagnostics and other observational facts. Then, we will proceed to explore more realistic models of composite stellar populations.

The traditional physical description of the evolution seen in the FP is the change in mass to light ratio expected in the redshift range  $z = 0 - 1.2$  for a simple (single-burst) stellar population (SSP) (the correspondence between  $d \log(M/L_B)/dz$  and redshift of formation  $z_f$  is shown in Figure 20). For early-type galaxies more massive than  $10^{11} M_{\odot}$ , the evolution implies a high redshift of formation,  $z_f > 2$ , whereas redshifts of formation as low as  $z_f = 1.2 - 1.3$  are adequate for the systems of lower effective mass.

A major result of our paper, however, is that the above description is too simplistic because various independent diagnostics available to us (see Section 5.6) indicate that a significant fraction of the early-type population with mass lower than  $10^{11} M_{\odot}$  has suffered recent/secondary star formation. Furthermore, a SSP redshift of formation of  $z_f \sim 1.2$  for lower mass objects would be impossible to reconcile with the results of deep infrared surveys (Glazebrook et al. 2004; Cimatti et al. 2004), which have found a substantial number of galaxies (including morphological E+S0; e.g., Stanford et al. 2004) with stellar mass above  $10^{10} M_{\odot}$  at redshift above 1.2.

A more appropriate representation is therefore a composite stellar population. Since subsequent bursts involving a relatively small fraction of stellar mass can substantially alter the evolution of the mass to light ratio (Trager et al. 2000; Treu et al. 2001), we will consider models where a (dominant) fraction of the stellar mass is old ( $z_{f1} > 2$ ) and the rest of the stellar mass was formed at  $z_{f2} < 1.2$ . We will show that these models provide a good description of the data and use them to derive limits on the fraction of younger stars.

This procedure is illustrated in Figure 21 where we compare the evolution of the mass-to-light ratio for families of simple two-burst models with that observed for our sample. Starting from the left panel panel we discuss E+S0 galaxies in order of decreasing mass. For

the most massive galaxies ( $> 10^{11.5} M_{\odot}$ ), the average evolution is well described by that of a very old stellar population formed at  $z_f = 5$ . Secondary burst at  $z_{f2} < 1.2$  are allowed but they cannot involve more than 1% of the total stellar mass. For intermediate mass objects (center panel), larger bursts are allowed, up to  $\sim 5\%$  of the stellar mass. For the smallest masses (right panel) bursts involving 10% of the stellar mass at  $z < 1.2$  are needed. For the largest masses these are solid upper limits and are consistent with, for example, accretion of small satellites. As discussed in T05 this is at variance with the expectations of a simple scheme where the growth of stellar mass follows the bottom-up growth of dark matter halos (see T05 for discussion).

For the less massive galaxies, however, when the mass in the secondary bursts starts to be a significant fraction of the total mass there is an additional complication. These larger secondary bursts are a quite dramatic event, which could be the result for example of a major merger, involving a rapid transformation of gas into stars. After such a dramatic event, it is unlikely that a galaxy would be recognizable morphologically until dynamical relaxation is complete (i.e. of order a Gyr after the event; c.f. van Dokkum & Franx 2001). Thus a more realistic estimate of the mass in these significant secondary bursts is obtained as in T05, assuming at least 1Gyr of age for the young population. In some cases, this requires fraction of mass in the young population as high as 20-40%.

### 5.5. Comparison with previous results

In the past few years, several groups have used the FP to investigate the evolution of the mass-to-light ratio of field spheroidal galaxies either using direct measurements of velocity dispersion (Treu et al. 1999, 2001a,b, 2002, 2005; van Dokkum et al. 2001; van Dokkum & Ellis 2003; Bernardi et al. 2003; Gebhardt et al. 2003; van der Wel et al. 2004) or estimating stellar velocity dispersions from the separation of multiple images of gravitationally lensed background objects (Kochanek et al. 2000; Rusin et al. 2003; van de Ven et al. 2003; Rusin & Kochanek 2005). The Lenses Structure and Dynamics (LSD) Survey (Koopmans & Treu 2002,2003; Treu & Koopmans 2002,2003,2004; hereafter collectively KT) measured stellar velocity dispersions of gravitational lenses thus bridging the gap between the two methods. For reference, previous measurements are summarized in Table 2.

The first thing to notice from the table is that all published measurements indicate faster FP evolution than that found for cluster galaxies ( $-0.49 \pm 0.05$ , van Dokkum et al. 1998) although in some cases the difference is not statistically significant. The second important point is that most measurements, even those based on lensing properties, agree with one another to within the quoted  $1-\sigma$  uncertainties. This can be explained by the structural

homogeneity of early-type galaxies which appear to have close to isothermal mass density profiles (e.g. Rusin et al. 2003b) as a result of a still unexplained dark- luminous matter conspiracy (e.g. Treu & Koopmans 2004).

If we take the measurement from this paper as the reference, all measurements listed in Table 2 are in agreement within the uncertainties except for van Dokkum & Ellis (2003) and Rusin et al. (2003) who measure a slightly slower evolution, and Gebhardt et al. (2003), whose work appears to indicate faster evolution. The latter discrepancy might be explained by a selection bias of the type shown in Figure 15, particularly since the Gebhardt et al study used considerably shorter exposure times at comparable redshifts. Other differences might be explained by the different mass ranges in the various samples, contamination by bulge-dominated spirals in shallower imaging data, or simply by small number statistics and different fitting techniques. If mass-to-light ratios follow the tracks illustrated in Figure 21, as a result of a series of secondary bursts overlayed on an old stellar population, the average evolutionary rate will depend on the fraction of objects caught in the active luminous phase. Similarly, different fitting techniques could be more or less sensitive to “outliers” and yield varied answers and error estimates. In short, small samples will be very sensitive to fluctuations in this number and to the adopted fitting technique.

Previous studies have often emphasized the differences between the results, arguing whether or not field early-type galaxies have younger stellar populations than their counterparts in clusters. Our sample allows us to firmly establish that field early-type galaxies have, on average, younger stellar populations than cluster galaxies, as a result of a more diverse star formation history, i.e. a wider range in epochs of star formation and secondary activity extended at relatively recent cosmic times.

## 5.6. Independent diagnostics of recent star formation

In T05 we showed that the mass-to-light ratio measured from the FP correlates well with the rest frame B-V color, indicating that deviations from the passive trend (defined in that paper by that observed for cluster early-types; and measured with the parameter  $\delta\Delta M/L_B$ , Section 5.1) is associated with younger stellar populations. In this Section, we will extend this analysis, using spectral ([O II] and H $\delta$ ) and morphological (blue cores) diagnostics as independent probes of the star formation history of our sample of E+S0 galaxies. We will use [O II] as an indicator of ongoing star formation (e.g. Kennicutt 1992), since the life time of the hot OB stars required to produce photo-ionizing photons is very short. Similarly, as strong H $\delta$  absorption occurs primarily in A stars with main sequence lifetimes of  $\sim 1$  Gyr, we use its occurrence to measure the recent activity.

Prior to using blue cores and emission lines as star formation diagnostics, we must consider what fraction of this activity might be due to non-thermal AGN. For this purpose we identify nuclear activity on the basis of X-ray luminosity as discussed in Section 4. Adopting a conservative threshold of  $L_X > 10^{42} \text{ erg s}^{-1}$ , we find only two of the 14 galaxies with blue cores are likely to be AGN dominant, with a further a possible LLAGN. Similarly, three strong [O II] emitters (i.e.  $\text{EW} > 15 \text{ \AA}$ ; 2 early-types, 1 Sa+b) without blue cores are identified as AGNs. These objects are excluded from the analysis in the rest of this section, guaranteeing that the remaining blue cores and [O II] are indeed due to star formation.

To visualize the connection between star formation indicators, morphology and mass to light ratio, we plot in Figure 22 the distribution of the offset from the redshift-dependence of the FP evolution of massive cluster spheroidals  $\delta\Delta M/L_B$  (Equation 11). Galaxies with signs of recent star formation (blue-cores, strong [O II] emitters, and  $\text{H}\delta$  equivalent widths  $< -3 \text{ \AA}$ ) show in general a larger offset than the quiescent population. However, even the quiescent population evolves more rapidly than the cluster population ( $\delta\Delta M/L_B \equiv 0$ ). Quantitatively, for the E+S0 galaxies, the average  $\delta\Delta M/L_B$  is  $-0.23 \pm 0.02$  for the entire sample,  $-0.39 \pm 0.07$  for the  $\text{H}\delta$  strong galaxies,  $-0.39 \pm 0.10$  for the star forming blue cores, and  $-0.17 \pm 0.12$  for the star forming [O II] emitters.

In conclusion, galaxies whose images and spectra reveal evidence for recent star formation have lower mass to light ratios at a given redshift than their quiescent counterparts. No significant difference is found for the sample of galaxies with [O II] emission, perhaps because of small number statistics (11 E+S0s, excluding the 2 AGN) or perhaps because of the different timescales ([O II] is a measure of instantaneous star formation, while  $M/L_B$  is a measure of integrated star formation). However, the fraction of [O II] E/S0 emitters (11/54) for which the line is visible with our spectroscopic setup is significantly higher than for early-type galaxies in the local field ( $\sim 0.05$  Treu et al. 2002), providing further evidence for enhanced star formation.

Studying the evolution of  $\text{H}\delta$  absorption we can obtain an independent check on our inferences based on the evolution of the mass to light ratio and perform an independent test of the secondary activity postulated in Section 5.3.1. In Figure 23 we show  $\text{H}\delta$  equivalent width vs. redshift for all E+S0 galaxies <sup>2</sup> and compare it with the predictions of our simple (thick red line) and composite population models (black dashed lines). We find that the distribution of rest-frame  $\text{H}\delta$  equivalent widths is inconsistent with any single burst model formed at high redshift and recent star formation activity is required. As for the  $M/L_B$ , the

---

<sup>2</sup>Note that  $\text{H}\delta$  is only visible for a subset of objects (74/163 E+S0s), i.e. when redshifted into the wavelength range covered by our spectrograph.

distribution is well-reproduced by a composite population where the bulk of stellar mass is formed at high redshift (e.g.  $z_{f1} \sim 3$ ) and on average 10 % of the stellar mass is added at a later time ( $z_{f2} \sim 0.5 - 1$ ) in secondary bursts.

Evidence for downsizing in the population, discussed initially by T05, is also seen in the H $\delta$  absorption. To illustrate this, coadded spectra of all the E+S0 galaxies binned in redshift and mass are shown in Figure 24. For galaxies with masses smaller than  $10^{11} M_{\odot}$  we find an average H $\delta$  equivalent width  $\sim -3 \text{ \AA}$ , inconsistent with the expected value for an old stellar population (c.f. Figure 24; see also van Dokkum & Ellis 2003 calculate  $\sim -1 \text{ \AA}$  for stellar populations formed at  $z \sim 3$  and observed at  $z \sim 0.9$ ).

## 6. Summary and conclusions

We have obtained ultra-deep spectroscopy of 163 field E+S0 and 61 bulge dominated Sa+b galaxies, selected morphologically from the GOODS-N field to a magnitude limit of  $z_9 < 22.43$ . Redshifts are measured for all objects in the sample, while stellar velocity dispersions are obtained for 141/163 E+S0s and 40/61 Sa+bs. The E+S0s with measured stellar velocity dispersion represent an unbiased and representative subsample of the parent morphological population. Structural parameters are obtained by fitting  $r^{1/4}$  profiles to the ACS images. Morphological asymmetries and blue cores are identified on the basis of the multicolor ACS images. Blue core spheroidals represent approximately 10% of the population (14/163). When visible with our spectroscopic setup, [O II] and H $\delta$  are measured and used as secondary star formation indicators.

Our redshift catalog is cross-correlated with the deep 2Ms X-ray catalog of the Chandra Deep Field North (Barger et al. 2003) to identify AGN and star forming galaxies. Nine E+S0s, including 2 blue cores, and 6 Sa+bs are identified as AGN based on an X-ray luminosity above  $10^{42} \text{ erg s}^{-1}$ . 21 additional galaxies (16 E+S0s, 4 Sa+bs, 1S) are also detected in the X-ray with luminosities between  $10^{40}$  and  $10^{42} \text{ erg s}^{-1}$ , which are interpreted as mostly due to a low luminosity AGN or to ongoing star formation. The vast majority (11/14) of blue core E+S0s are not detected in the deep Chandra exposures, indicating that the blue cores are the result of spatially concentrated star formation activity, and not of non thermal AGN emission.

We study the evolution of the Fundamental Plane as a diagnostic of the star formation and mass assembly history of early-type galaxies, using Montecarlo simulations to rigorously control selection effects. The main results can be summarized as follows:

1. The mass-to-light ratio of field spheroidals evolves on average as  $d \log(M/L_B)/dz =$



$-0.72^{+0.07}_{-0.05} \pm 0.04$ , i.e. faster than that of cluster spheroidals ( $-0.49 \pm 0.05$  van Dokkum et al. 1998). This is consistent with the stellar population of field spheroidals being on average younger. Although the difference between the FP evolution of cluster and field spheroidals (Table 2) is in the sense expected by hierarchical models (Diaferio et al. 2001; De Lucia et al. 2004), quantitatively it is not as pronounced as expected (van Dokkum et al. 2001; Treu 2004).

2. The evolution of the Fundamental Plane, and thus of the effective mass to light ratio, depends strongly on mass: the less massive the galaxy, the faster the evolution. The mass-to-light ratio of the most massive galaxies ( $> 10^{11.5} M_{\odot}$ ) evolve as that of an old stellar population ( $z_f > 2$ ), with an upper limit of  $\sim 1\%$  to the fraction of stellar mass that can have formed at  $z < 1.2$ . The evolution of the mass to light ratio of the less massive galaxies is inconsistent with that of a single burst stellar population. A significant fraction of the mass (up to 20-40 % for masses below  $10^{11} M_{\odot}$ ) must have formed more recently than  $z_{f2} = 1.2$  consistent with significant recent growth of this population.
3. The intrinsic scatter of the FP is found to increase with redshift, after allowing for evolution of the slopes, as  $d\text{rms}(\log M/L_B)/dz = 0.040 \pm 0.015$ , consistent with the idea that we have approached an epoch of starformation activity in this population.
4. The scenario of mass dependent star formation history and significant recent growth for E+S0 with mass below  $10^{11} M_{\odot}$  is supported by independent star formation indicators. The mass-to-light ratio of spheroidal galaxies with blue rest frame colors (discussed in a companion paper, T05), strong emission or balmer absorption ([O II] and H $\delta$ ), and morphological anomalies (blue cores) is found to evolve more rapidly than that of quiescent galaxies. The fraction of E+S0s galaxies with [O II] emission is larger (13/54, or 11/54 excluding two emitters identified as AGN based on the X-ray emission) than in the local universe ( $\sim 0.05$ ; Treu et al. 2002). The distribution of H $\delta$  absorption for our sample is well reproduced by the same two-bursts models describing the evolution of the FP.

We promote, therefore, a picture in which all spheroidals except the most massive ones continue to assemble and form young stars via subsequent episodes of star formation. The associated rejuvenation is sufficient to significantly influence the location of the galaxy on the FP and, of course, its colors. As a result, a fraction of spheroidal galaxies will have blue colors, and be missed in color selected samples (e.g. Jimenez et al. 1999). Likewise, passive models will be an inadequate representation of the evolutionary behavior. Introducing secondary bursts implies that for a given luminosity function (or equivalently observed surface density;

Im et al. 2002; Cross et al. 2004) will lead to an increased evolutionary rate in the number density evolution (Treu 2004).

Ultimately we seek to connect the evolution of the mass to light ratio for various masses with the broader issue of how the *number* of spheroidals is growing with cosmic time (c.f. Franx 1993). To illustrate a possible approach to this important larger picture, we explore combining the FP measurements made in this paper with constraints on the evolution of the luminosity function (LF), for example morphologically-selected E+S0s from the WFPC2 survey discussed by Im et al (2002).

Im et al. (2002) chose to represent the evolution of their E+S0 LF with two parameters:  $Q$  describing the luminosity evolution (equivalent to  $-2.5d \log(M/L_B)/dz$ ), and  $m$  describing the number density evolution, i.e. the characteristic density parameter in the Schechter (1976) luminosity function which is postulated to evolve as  $(1+z)^m$ . With luminosity function data alone, there is a degeneracy between  $Q$  and  $m$ : stronger luminosity evolution implies a stronger number density evolution. Using our measured value for the luminosity evolution inferred independently from the FP (equivalent to  $Q = 1.80 \pm 0.15$ ) in combination with the  $\chi^2$  surface shown in their Figure 24, we eliminate the degeneracy and obtain  $m = -0.6 \pm 0.5$ .

This value of  $m$  implies an abundance of morphologically selected E+S0s at  $z \sim 1.2$  of  $60^{+30}_{-20}$  % of the local value. If correct, the decline in the number density of red galaxies (Bell et al. 2004) would be explained in part by an evolution of the number density of E+S0s galaxies (at least those morphologically identifiable, e.g., van Dokkum & Franx 2001) and in part by their blue colors. Such an interpretation would apply equally to samples of color- and morphologically- selected higher redshift E+S0 galaxies (Menanteau et al. 1999; Treu & Stiavelli 1999; Stanford et al. 2004).

Although a crude resolution of the differences seen for the various datasets, largely because of the uncertainties in combining different datasets and the limited size (and thus cosmic variance noise) of the Im et al. 2002 sample, by combining of our precise FP measurements with more extensive luminosity functions a more robust empirical picture of the evolution of E+S0s in the last 9 Gyrs can be determined.

The use of the Gauss-Hermite Pixel Fitting Software developed by R. P. van der Marel is acknowledged. Financial support by NASA (Hubble Fellowship HF-01167.01; STScI-AR-09960) and NSF (AST-0307859) is acknowledged. We thank Kevin Bundy for his help in developing the morphological classification catalog and for numerous scientific conversations. We thank those who developed DEIMOS and the staff of the Keck Observatory for making this project possible and the DEEP2 team for encouragement and helpful discussion. In particular, we would like to thank Greg Wirth, Chris Willmer and the Keck GOODS team

for kindly providing the self-consistent astrometric solution that was used to design the slit-masks, and Sandy Faber and David Koo for scientific discussions. We acknowledge helpful discussions with B. Abraham, M. Bernardi, G. Bertin, K. Glazebrook, S. Gallagher, X. Hernandez, S. Pellegrini, A. Renzini, S. White. We are grateful to Myunshin Im for providing his  $\chi^2$  surface in digital format. This paper is based on data obtained with the HST operated by AURA for NASA and the W.M. Keck Observatory on Mauna Kea, Hawaii. The W.M. Keck Observatory by the California Institute of Technology, the University of California and NASA and was made possible by the generous financial support of the W.M. Keck Foundation.

## REFERENCES

- Abraham, R.G., van den Bergh, S., Glazebrook, K., Ellis, R.S., Santiago, B.X., Surma, P., Griffiths, R.E. 1996, ApJS, 107, 1
- Alexander, D.M. et al. 2003, AJ, 126, 539
- Barger, A.J. et al. 2003, AJ, 126, 632
- Baugh, C.M., Cole, S., Frenk, C.S., Lacey, C.G. 1998, ApJ, 498, 504
- Bell, E. et al. 2004, ApJ, 608, 752
- Bender R., Burstein D., Faber S. M., 1992, ApJ, 399, 462
- Bernardi M., et al. 2003, AJ, 125, 1866
- Bernardi, M., Nichol, R.C., Sheth, R.K., Miller, C.J., Brinkmann J., 2005, ApJ, submitted
- Bender, R., Saglia, R. P., Ziegler, B., Belloni, P., Greggio, L., Hopp, U., Bruzual, G., 1998, ApJ, 493,
- Benson, A.J., Ellis, R.S. & Menanteau, F. 2002, MNRAS, 336, 564
- Blain, A.W., Smail, I., Ivison, R.J., Kneib, J.-P. 1999, MNRAS, 307, 480
- Bower R. G., Lucey J. R., Ellis R. S., 1992, MNRAS, 254, 601
- Brinchmann, J. & Ellis, R.S. 2000, ApJ, 536, L77
- Bunker, A.J., Stanway, E.R., Ellis, R.S., McMahon, R.G. 2004, MNRAS, 355, 374
- Bundy, C.K., Ellis, R.S., Conselice, C.J. 2005, ApJ, in press, astro-ph/0502204

- Chapman, S.C., Smail, I., Blain, A.W., Ivinson, R.J. 2004, ApJ, 614, 671
- Cimatti, A. et al., 2004, Nature, 430, 184
- Ciotti, L., Lanzoni, B., Renzini A. 1996, MNRAS, 282, 1
- Cohen, J.G. 2002, ApJ, 567, 672
- Coil, A. et al. 2004, ApJ, 609, 525
- Cowie L.L., Songaila, A., Hu, E.M., Cohen J.G. 1996, AJ, 112, 839
- Cross, N.J. et al. 2004, AJ, 128, 1990
- Davis, M. et al. 2003, SPIE, 4834, 161
- De Lucia, G., Kauffmann, G., & White, S.D.M. 2004, MNRAS, 349, 1101
- Diaferio, A., Kauffmann, G., Balogh, M.L., White, S.D.M., Schade, D., Ellingson, E. 2001, MNRAS, 323, 999
- Djorgovski S. G., Davis M., 1987, ApJ, 313, 59
- Dressler, A. 1980, ApJ, 236, 351
- Dressler, A., Lynden-Bell, D., Burstein, D., Davies, R. L., Faber, S. M., Terlevich, R., Wegner G. 1987, ApJ, 313, 42
- Ellis, R.S., Smail I., Dressler, A., Couch, W. J., Oemler, A., Butcher, H., Sharples, R. M., 1997, ApJ, 483, 582
- Faber S. M., Dressler A., Davies R. L., Burstein D., Lynden-Bell D., 1987, in Faber S. M., ed., *Nearly Normal Galaxies*. Springer, New York, p .175
- Fisher, D., Fabricant, D., Franx, M., van Dokkum, P.G. 1998, 498, 195
- Fontana, A., et al. 2004, A&A, 424, 23
- Franx, M. 1993, PASP, 105, 1058
- Fukugita, M., Ichikawa, T., Gunn, J.E., Doi, M., Shimasaku, K., Schneider, D.P. 1996, AJ, 111, 1748
- Giavalisco, M. et al. 2004, ApJ, 600, L93
- Glazebrook, K. et al. 2004, Nature, 430, 181

- Gebhardt, K. et al. 2003, ApJ, 597, 239
- Hernandez, X. & Lee, W.H., 2004, MNRAS, 347, 1304
- Im, M. et al. 2002, ApJ, 571, 136
- Jimenez R., Friaca A. C. S., Dunlop J. S., Terlevich R. J., Peacock J. A., Nolan L. A., 1999, MNRAS, 305, L16
- Jimenez, R. Panther, B., Heavens, A., & Verde, L. 2004, MNRAS, in press
- Jorgensen, I., Franx, M., Kjaergaard, P. 1992, A&A, 95, 489
- Jorgensen, I., Franx, M., Kjaergaard, P. 1996, MNRAS, 280, 167
- Kauffmann, G. 1996, MNRAS, 281, 478
- Kelson, D. D., van Dokkum, P. G., Franx, M., Illingworth G. D., & Fabricant, D. G. M. 1997, ApJ, 478, L13
- Kelson, D.D., Illingworth, G.D., van Dokkum, P.G. & Franx, M. 2000, ApJ, 531, 137
- Kelson, D.D., Illingworth, G.D., van Dokkum, P.G. & Franx, M. 2000, ApJ, 531, 159
- Kelson, D.D., Illingworth, G.D., van Dokkum, P.G. & Franx, M. 2000, ApJ, 531, 184
- Kennicutt R. 1992, ApJ, 388, 310
- Kim, D.W., & Fabbiano, G. 2004, ApJ, 611, 846
- Lanzoni, B., Ciotti, L., Cappi, A., Tormen, G., Zamorani, G. 2004, 600, 640
- Madau, P., Ferguson, H.C., Dickinson, M. E., Giavalisco, M., Steidel, C.C., Fruchter, A. 1996, MNRAS, 283, 1388
- Menanteau, F., Ellis, R. S., Abraham, R. G., Barger, A. J., & Cowie, L. L. 1999, MNRAS, 309, 208
- Menanteau, F., Abraham, R.G., Ellis, R.S. 2001, MNRAS, 322, 1
- Menanteau, F., Jimenez, R., Matteucci, F. 2001, ApJ, 562, L23
- Menanteau, F. et al. 2004, ApJ, 612, 202
- Menanteau, F. et al. 2005, ApJ, 620, 697

- McCarthy, P. J. 2004, ARA&RA, 42, 477
- Oke, J. B. 1974, ApJS, 27, 21
- O’Sullivan, E., Forbes, D.A., & Ponman, T. 2001, MNRAS, 328, 461
- O’Sullivan, Ponman, T., & Collins, R.S. 2003, MNRAS, 340, 1375
- Pahre M. A., 1998, PhD Thesis, California Institute of Technology
- Papovich, C., Dickinson, M.E., Ferguson, H.C. 2001, ApJ, 559, 620
- Pellegrini, S. & Ciotti, L. 1998, A&A, 333, 433
- Peng, C., Ho, L.C., Impey, C.D., Rix, H.-W. 2002, AJ, 124, 266
- Ranalli, P., Comastri, A., Setti, G. 2003, A&A, 399, 39
- Rudnick, G. et al. 2003, ApJ, 599, 847
- Rusin, D. & Kochanek, C.S. 2005, ApJ, submitted, astro-ph/0412001
- Rusin, D. et al. 2003a, ApJ, 587, 143
- Rusin, D., Kochanek, C.S., Keeton, C.R. 2003b, ApJ, 595, 29
- Schechter, P., 1976, ApJ, 203, 297
- Somerville, R. & Primack 1999, MNRAS, 310, 1087
- Stanford, S. A., Dickinson, M., Postman, M., Ferguson, H.C., Lucas, R.A., Conselice, C.J., Budavri, T., Somerville, R. 2004, AJ, 127, 131
- Steidel, C.C., Adelberger, K.L., Giavalisco, M., Dickinson, M.E. & Pettini, M. 1999, ApJ, 519, 1
- Trager, S. C., Worthey, G., Faber, S. M., Burstein, D., Gonzalez, J. J. 1998, ApJS, 116, 1
- Trager S. C., Faber S. M., Worthey G., Gonzalez J. J., 2000, AJ, 119, 1645
- Treu T. 2001, Ph. D Thesis, Scuola Normale Superiore.
- Treu, T. 2004, Carnegie Observatories Astrophysics Series, Vol. 3: Clusters of Galaxies: Probes of Cosmological Structure and Galaxy Evolution, ed. J. S. Mulchaey, A. Dressler, and A. Oemler (Cambridge: Cambridge Univ. Press)

- Treu, T. & Koopmans, L. V. E. 2002, *ApJ*, 575, 87
- Treu, T. & Koopmans, L. V. E. 2004, *ApJ*, 611, 739
- Treu, T., Stiavelli, M., Casertano, C., Møller, P., & Bertin G. 1999, *MNRAS*, 308, 1307
- Treu, T., Stiavelli, M., Møller, P., Casertano, C., & Bertin G. 2001a, *MNRAS*, 326, 221
- Treu, T., Stiavelli, M., Bertin G., Casertano, C., & Møller, P. 2001b, *MNRAS*, 326, 237
- Treu, T., Stiavelli, M., Casertano, C., Møller, P., Bertin, G. 2002, *ApJ*, 564, L13
- Treu, T., Ellis, R.S, Kneib, J.-P., Dressler, A., Smail, I., Czoske, O., Oemler, A. & Natarajan, P. 2003, *ApJ*, 591, 53
- van de Ven, G., van Dokkum, P.G. & Franx, M. 2003, *MNRAS*, 344, 924
- van der Marel, R. 1994, *MNRAS*, 270, 271
- van der Wel, A., Franx, M., van Dokkum, P.G. & Rix, H.-W. 2004, *ApJ*, 601, L5
- van Dokkum, P.G. & Ellis, R.S. 2003, *ApJ*,
- van Dokkum P.G., Franx M., 1996, *MNRAS*, 281, 985
- van Dokkum P.G., Franx M., 2001, *ApJ*, 553, 90
- van Dokkum, P.G., Stanford, S.A. 2003,
- van Dokkum, P. G., Franx, M., Kelson D. D. & Illingworth, G. D., 2001, *ApJ*, 553, L39
- van Dokkum, P.G. et al. 2004, *ApJ*, 611, 703
- Wirth, G. et al. 2004, *AJ*, 127, 3121
- Wuyts, S., van Dokkum, P. G., Kelson, D. D., Franx, M., Illingworth, G. D., 2004, *ApJ*, 605, 677

Table 1. Catalog of spheroidals and bulge dominated galaxies

| ID   | RA        | DEC      | T | $b_4$ | $r_{e4}$ | $v_6$ | $r_{e6}$ | $i_8$ | $r_{e8}$ | $z_9$ | $r_{e9}$ | $z$    | $\sigma_{ap}$ | [O II]         | H $\delta$     | S/N | $t_{exp}$ |
|------|-----------|----------|---|-------|----------|-------|----------|-------|----------|-------|----------|--------|---------------|----------------|----------------|-----|-----------|
| 1287 | 189.13248 | 62.15182 | 0 | -     | -        | 21.90 | 0.81     | 20.80 | 0.45     | 19.95 | 0.47     | 0.8457 | 319 $\pm$ 22  | -0.4 $\pm$ 0.3 | 1.3 $\pm$ 0.2  | 22  | 19800     |
| 648  | 189.16547 | 62.13849 | 0 | 22.30 | 0.76     | 21.21 | 0.37     | 20.58 | 0.29     | 20.24 | 0.28     | 0.2469 | 65 $\pm$ 13   | -              | -              | 26  | 19130     |
| 609  | 189.19130 | 62.10799 | 0 | -     | -        | 22.45 | 0.74     | 21.09 | 0.55     | 20.51 | 0.49     | 0.7976 | 247 $\pm$ 16  | 5.4 $\pm$ 0.6  | -2.2 $\pm$ 0.4 | 12  | 19130     |
| 1286 | 189.13710 | 62.15260 | 2 | -     | -        | 22.41 | 1.21     | 21.06 | 0.85     | 20.36 | 0.76     | 0.8461 | 231 $\pm$ 16  | -0.6 $\pm$ 0.6 | 1.7 $\pm$ 0.4  | 12  | 19800     |
| 655  | 189.19568 | 62.13973 | 1 | -     | -        | 21.91 | 0.78     | 20.72 | 0.81     | 20.35 | 0.75     | 0.6421 | 99 $\pm$ 7    | -              | 3.7 $\pm$ 0.4  | 14  | 19130     |
| 1253 | 189.13830 | 62.14290 | 3 | -     | -        | 22.23 | 0.03     | 21.90 | 0.03     | 21.24 | 0.10     | 0.9349 | -             | 3.8 $\pm$ 0.2  | 1.8 $\pm$ 0.2  | 18  | 19800     |
| 1236 | 189.13470 | 62.13730 | 0 | -     | -        | 22.91 | 0.61     | 21.59 | 0.40     | 20.92 | 0.35     | 0.8503 | 202 $\pm$ 11  | 0.5 $\pm$ 0.4  | -2.0 $\pm$ 0.3 | 14  | 37800     |
| 1278 | 189.15150 | 62.14850 | 2 | -     | -        | 22.51 | 0.14     | 21.57 | 0.12     | 21.19 | 0.12     | 0.5125 | 108 $\pm$ 7   | -              | -              | 22  | 37800     |
| 681  | 189.16202 | 62.15102 | 1 | -     | -        | 23.28 | 0.40     | 21.87 | 0.34     | 21.17 | 0.32     | 0.8422 | 318 $\pm$ 28  | -0.7 $\pm$ 0.5 | -0.3 $\pm$ 0.3 | 13  | 38930     |
| 635  | 189.20297 | 62.12884 | 2 | -     | -        | 23.24 | 0.59     | 21.73 | 0.45     | 21.05 | 0.41     | 0.8195 | 187 $\pm$ 16  | -0.5 $\pm$ 0.5 | -2.1 $\pm$ 0.4 | 11  | 38930     |

Note. — For each object we list ID, RA, DEC, morphological type, AB magnitudes (from  $r^{1/4}$  fitting) and effective radii (in arcsec), redshifts, measured velocity dispersion  $\sigma_{ap}$  in  $\text{km s}^{-1}$ , [O II] and H $\delta$  equivalent widths (in  $\text{\AA}$ , rest frame), average signal-to-noise ratio ( $\text{\AA}^{-1}$ ; observer frame) and spectroscopic exposure time (in seconds). Photometric parameters through the  $b_4$  filter are derived only for objects at  $z < 0.34$ . Formal galfit uncertainties on magnitudes and effective radii are 0.01-0.02 mags and a 1-10% in effective radii. Total uncertainties on the combination of photometric parameters that enters the Fundamental Plane  $\log R_e - 0.32\text{SB}_e$  are 0.02-0.03. The Table is published in its entirety online, the first 10 entries are shown here for guidance.



Table 2. Summary of previous field measurements

| $d \log(M/L_B)/dz$               | $b_{\text{Redshift}}$ | sample | Source                  | Notes  |
|----------------------------------|-----------------------|--------|-------------------------|--|
| $-0.50 \pm 0.19$                 | 0.0-1.0               | 22     | Rusin & Kochanek 2005   | lensing-general; lenses                      |
| $-0.54 \pm 0.06$                 | 0.6-1.0               | 9      | van Dokkum & Ellis 2003 | direct; morphology and magnitude             |
| $-0.56 \pm 0.04$                 | 0.0-1.0               | 27     | Rusin et al. 2003       | lensing-isothermal; lenses                   |
| $-0.59 \pm 0.15$                 | 0.2-0.6               | 18     | van Dokkum et al. 2001  | direct; morphology and magnitude             |
| $-0.62 \pm 0.13$                 | 0.0-1.0               | 26     | van de ven et al. 2003  | lensing-isothermal; lenses                   |
| $-0.71 \pm 0.19$                 | 0.6-1.1               | 6      | van der Wel et al. 2004 | direct; morphology, magnitude and color      |
| $-0.72^{+0.16}_{-0.11}$          | 0.1-0.7               | 30     | Treu et al. 2002        | direct; morphology, magnitude and color      |
| $-0.72 \pm 0.10$                 | 0.5-1.0               | 5      | Treu & Koopmans 2004    | direct; lenses, early-types only             |
| $-0.75 \pm 0.17$                 | 0.5-1.0               | 5      | Treu & Koopmans 2004    | lensing-isothermal; lenses, early-types only |
| $-0.80..-96$                     | 0.3-1.0               | 36     | Gebhardt et al. 2003    | direct; magnitude and absorption lines       |
| $-0.72^{+0.07}_{-0.05} \pm 0.04$ | 0.2-1.2               | 141    | this work               | direct; morphology and magnitude             |

Note. — In the notes column, “direct” refers to spectroscopically determined velocity dispersions, “lensing-isothermal” refers to velocity dispersion estimate from image separation using an isothermal model, “lensing-general” refers to velocity dispersion estimate from image separation using a more general model (see Rusin & Kochanek 2005); the measurements for Gebhardt et al. 2003 are the average brightening to  $z = 0.8$  and  $z = 1.0$ , respectively.

### A. Transformations from ACS magnitude to rest frame B and V magnitudes

Throughout this paper, rest frame Landolt B and V magnitudes are obtained from the two ACS filters which are closest to the redshifted B and V central wavelengths (i.e. 4405 and 5470 Å, e.g., Fukugita et al. 1996). Given the redshift interval considered here  $0 < z < 1.25$ , a pair of ACS filters is always sufficient to obtain rest frame B and V magnitudes within few hundreds of magnitudes. Hence, the transformations adopted here can be expressed in the form:

$$B = v_6 + \alpha_{Bvbv}(b_4 - v_6) + \beta_{Bvbv} - DM \quad [0 \leq z < 0.34] \quad (A1)$$

$$B = i_8 + \alpha_{Bivi}(v_6 - i_8) + \beta_{Bivi} - DM \quad [0.34 < z \leq 0.76] \quad (A2)$$

$$B = z_9 + \alpha_{Bziz}(i_8 - z_9) + \beta_{Bziz} - DM \quad [0.76 \leq z < 1.25] \quad (A3)$$

$$V = v_6 + \alpha_{Vvbv}(b_4 - v_6) + \beta_{Vvbv} - DM \quad [0 \leq z < 0.07] \quad (A4)$$

$$V = i_8 + \alpha_{Vivi}(v_6 - i_8) + \beta_{Vivi} - DM \quad [0.07 < z \leq 0.41] \quad (A5)$$

$$V = z_9 + \alpha_{Vziz}(i_8 - z_9) + \beta_{Vziz} - DM \quad [0.41 \leq z < 1.25] \quad (A6)$$

where the coefficients  $\alpha$  and  $\beta$  are a function of redshift, while the bolometric distance modulus DM is a function of redshift and cosmography. Polynomial expansions of the coefficients are given in Table 3.

| N | $\alpha_{\text{Bv bv}}$ | $\beta_{\text{Bv bv}}$ | $\alpha_{\text{Bi vi}}$ | $\beta_{\text{Bi vi}}$ | $\alpha_{\text{Bz iz}}$ | $\beta_{\text{Bz iz}}$ |
|---|-------------------------|------------------------|-------------------------|------------------------|-------------------------|------------------------|
| 0 | 0.824411                | -0.00169895            | 2.44316                 | 0.748236               | 1491.01                 | -796.805               |
| 1 | -3.29360                | 1.22223                | -4.42301                | -3.72483               | -8947.85                | 4776.19                |
| 2 | 3.40645                 | -8.36258               | 1.53361                 | 7.43317                | 22264.2                 | -11813.0               |
| 3 |                         | 18.9313                |                         | -3.58153               | -29340.5                | 15426.2                |
| 4 |                         |                        |                         |                        | 21564.4                 | -11200.7               |
| 5 |                         |                        |                         |                        | -8367.60                | 4278.26                |
| 6 |                         |                        |                         |                        | 1336.45                 | -669.418               |
| N | $\alpha_{\text{Vv bv}}$ | $\beta_{\text{Vv bv}}$ | $\alpha_{\text{Vi vi}}$ | $\beta_{\text{Vi vi}}$ | $\alpha_{\text{Vz iz}}$ | $\beta_{\text{Vz iz}}$ |
| 0 | 0.186741                | -0.0274962             | 1.42588                 | -0.0394309             | -77.0651                | 46.5707                |
| 1 | -2.62562                | 0.995802               | -5.13394                | 1.23626                | 668.581                 | -399.767               |
| 2 | 7.19822                 | 0.0925006              | 4.22521                 | -1.42416               | -2294.21                | 1398.85                |
| 3 |                         |                        |                         | 1.88833                | 4056.19                 | -2539.31               |
| 4 |                         |                        |                         |                        | -3936.67                | 2531.96                |
| 5 |                         |                        |                         |                        | 1999.86                 | -1319.01               |
| 6 |                         |                        |                         |                        | -417.432                | 281.589                |

Table 3: Taylor expansion coefficients of  $\alpha$  and  $\beta$  around redshift  $z = 0$ . Redshift intervals of validity are given in Equations A1 to A6

## B. X-ray-based classification scheme

In this paper we adopted a simplified classification scheme, based on X-ray luminosity, to identify galaxies with nuclear activity (XAGN), or with low luminosity nuclear activity and/or ongoing star formation (XSF/LLAGN). The working definitions of AGN or XSF/LLAGN – admittedly schematic – are motivated by local studies of early-type galaxies which show that typically an AGN is required to power a luminosity above  $10^{42}$  erg s $^{-1}$  (with the exception of cluster brightest cluster galaxies – not present in our sample – where the ICM can reach these luminosities e.g. Pellegrini & Ciotti 1998, O’Sullivan, Forbes & Ponman 2001). At fluxes below  $10^{42}$  erg s $^{-1}$  the main contributors to the X-ray luminosities are LLAGNs, star formation related phenomena such as HMXB, low-mass X-ray binaries (LMXB), and emission from the diffuse plasma, with typical temperatures below 1 keV.

We can estimate the contribution of the two latter mechanisms as follows. The contributions from LMXB is proportional to the stellar mass and thus scales linearly with the B-band luminosity and it is generally small with respect to the total X-ray emission observed in local early-type galaxies (see O’Sullivan, Forbes & Ponman 2001; Kim & Fabbiano 2004). Using the relation from Kim & Fabbiano  $L_X$  (LMXB) =  $(0.9 \pm 0.5) 10^{30}$  erg s $^{-1}$   $L_B / L_{B,\odot}$  and our measured  $L_B$  we find that for our sample<sup>3</sup> the median contribution of LMXBs to the total X-ray emission is  $16 \pm 9\%$ .

As far as diffuse plasma emission is concerned, we can conservatively estimate its contribution by using the empirical scaling of the total soft X-ray luminosity with  $L_B$  as measured for E+S0 galaxies in the local universe, excluding AGN hosts and brightest cluster galaxies. Since local early-type galaxies are mostly quiescent, the excess with respect to the local relationship provides an estimate of the contribution due to star formation or LLAGN in high redshift sources. For example O’Sullivan, Ponman & Collins (2003) find  $L_{0.5-2} \simeq 4 \times 10^{41} \times (L_B/10^{11})^{2.7}$ , albeit with a scatter of an order of magnitude. Applied to our sample, this relationship results in an expected X-ray luminosity corresponding to  $6 \pm 4\%$  of the total observed one. As an example of the uncertainty in this estimate, adopting instead the relationship in Eq.1 from O’Sullivan, Forbes & Ponman (2001) raises the fraction to  $25 \pm 15\%$ . We conclude that in general the X-ray luminosity of our distant E+S0 with luminosities in the range  $10^{40}$ - $10^{42}$  erg s $^{-1}$  is due largely to star formation and/or LLAGN and cannot be explained entirely by the plasma and LMXB emission expected for local E+S0. However, given the high intrinsic scatter of the local relationships, XSF/LLAGN might not be needed in some individual cases.

---

<sup>3</sup> $\log L_B/L_{B,\odot}$  is in the range 9.2-10.8 average 10.2, after evolving to  $z = 0$  using the evolution of the FP measured in Section 5.

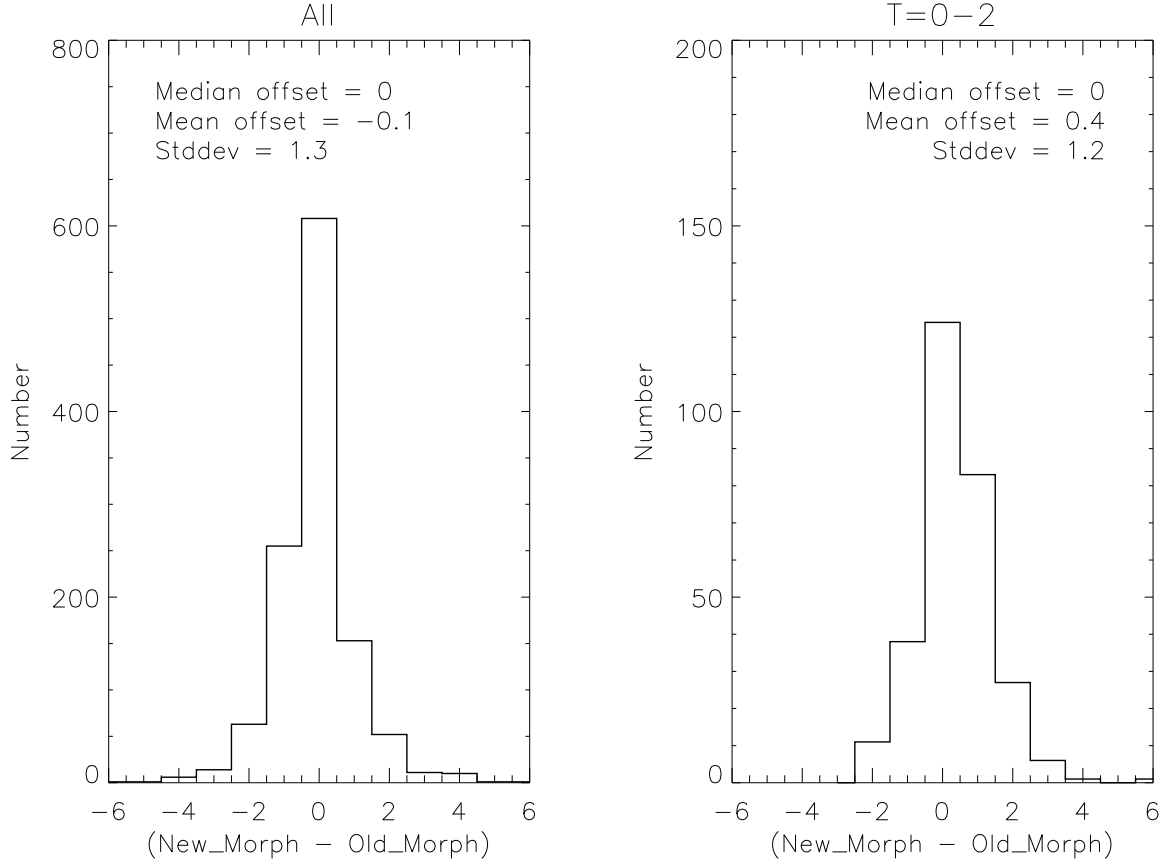


Fig. 1.— Comparison of morphological classifications based on the v0.5 and v1.0 releases of the GOODS data, referred to as “old” and “new” respectively. Types T are assigned based on the following scheme: T=-2=star, -1=compact, 0=E, 1=E/S0, 2=S0, 3=Sa+b, 4=S, 5=Sc+d, 6=Irr, 7=Unclass, 8=Merger, 9=Fault (Abraham et al. 1996; Treu et al. 2003). Left panel refers to all classes, right to spheroidals only.

Fig. 2.— Color-composite images ( $R=z_9$ ,  $G=i_8$ ,  $B=v_6$ ) of all early-type galaxies in the Keck spectroscopic sample, sorted by redshift. The color scheme is chosen so that a local early-type galaxy would appear white. Images are  $3''$  on a side. For each galaxy redshift, ID, and morphological type are shown in the upper left, lower left and lower right corner respectively.

Fig. 2.— Color-composite images of all early-type galaxies (continued).

Fig. 2.— Color-composite images of all early-type galaxies (continued).

Fig. 3.— Color-composite images ( $R=z_9$ ,  $G=i_8$ ,  $B=v_6$ ) of all the early-spirals in the Keck spectroscopic sample, sorted by redshift.

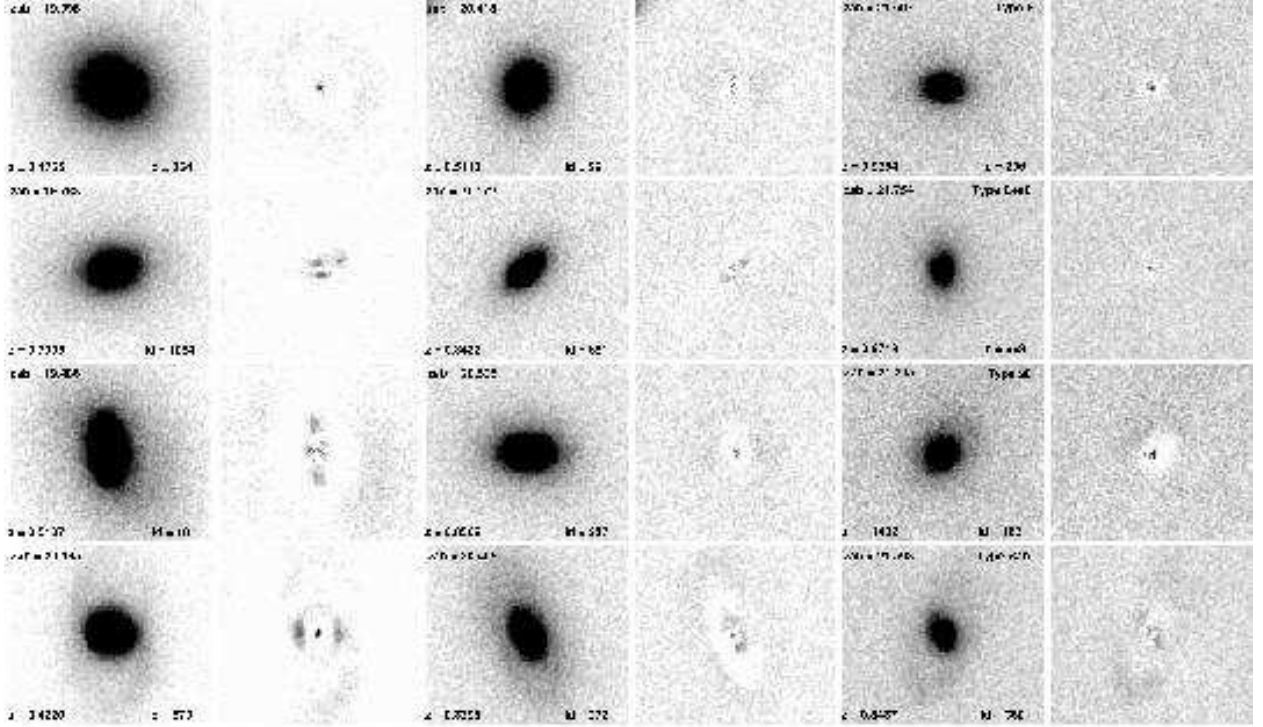


Fig. 4.— Examples of de Vaucouleurs fits: for galaxy types  $-1 < T < 4$  (one per row), for three different magnitude bins,  $z \sim 20$ ,  $z \sim 21$ ,  $z \sim 22$ . For each galaxy the original image is shown alongside residuals from the best fit  $r^{1/4}$  model. Notice the disk-like residuals in the S0 galaxies and the spiral arm residuals in the Sa+b galaxies confirming the v1.0 visual classification. Redshift, magnitude and ID are listed for each object. Each panel is  $3''.0 \times 2''.7$ .

Fig. 5.— Montage of 'blue core' early type galaxies, selected as defined in the text, sorted by redshift. Each image is  $3''$  on a side. Only the two highest redshift examples appear to host active galactic nuclei, as indicated by the large X-ray luminosity ( $> 10^{42} \text{ erg s}^{-1}$ ). The bulk of the blue light arises from recent star formation.

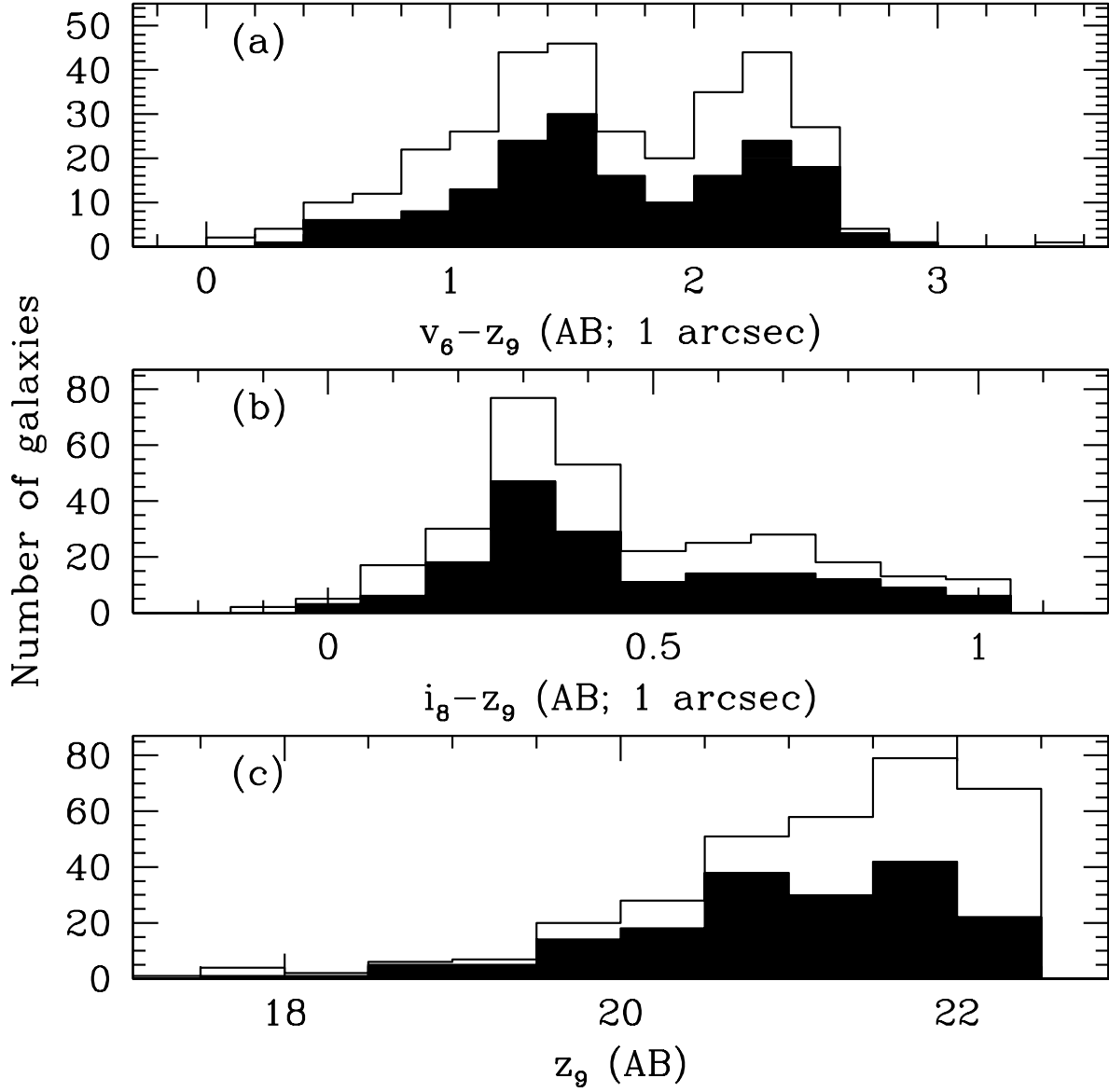


Fig. 6.— Distribution of colors (panels a and b) and  $z_9$  magnitudes (panel c) for the full sample of  $z_9 < 22.43$  E+S0 galaxies classified in the final v1.0-zcatalog (empty histogram) compared to the E+S0 sample (v1.0 morphologies) targeted for spectroscopy (solid histogram). The sampling rate is approximately independent of color, but drops off beyond  $z_9 \sim 21.5$  as discussed in Section 3.1.



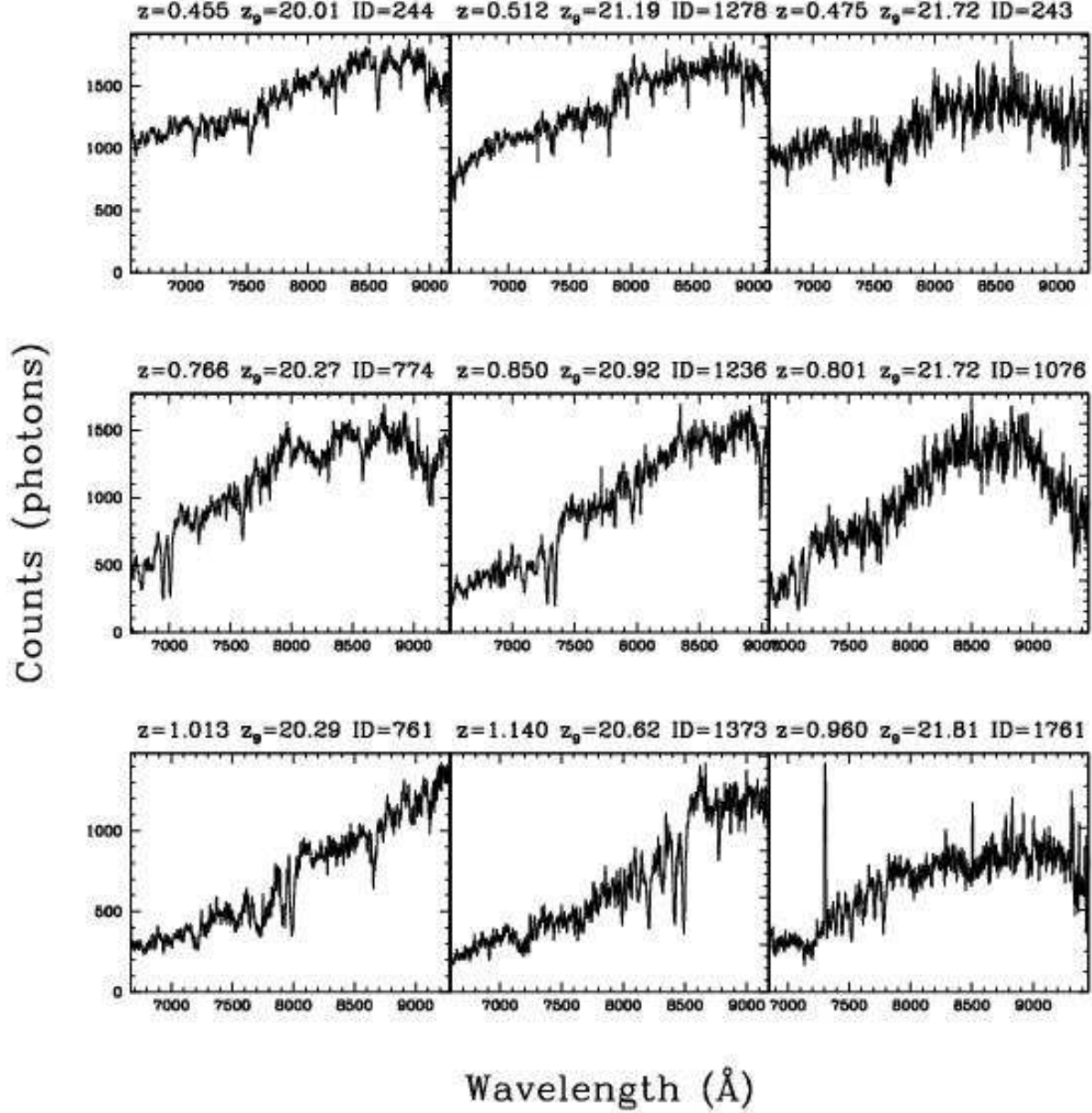


Fig. 7.— Examples of flux-calibrated spectra – smoothed with a boxcar filter of width  $6\text{\AA}$ – for three different magnitude bins,  $z_9 \sim 20$ ,  $z_9 \sim 21$ ,  $z_9 \sim 22$  and redshifts ( $z \sim 0.5, z \sim 0.8, z \sim 1$ ). The signal-to-noise ratio decreases with magnitude and exposure time as expected. Fluxes are in units proportional to photons per second.

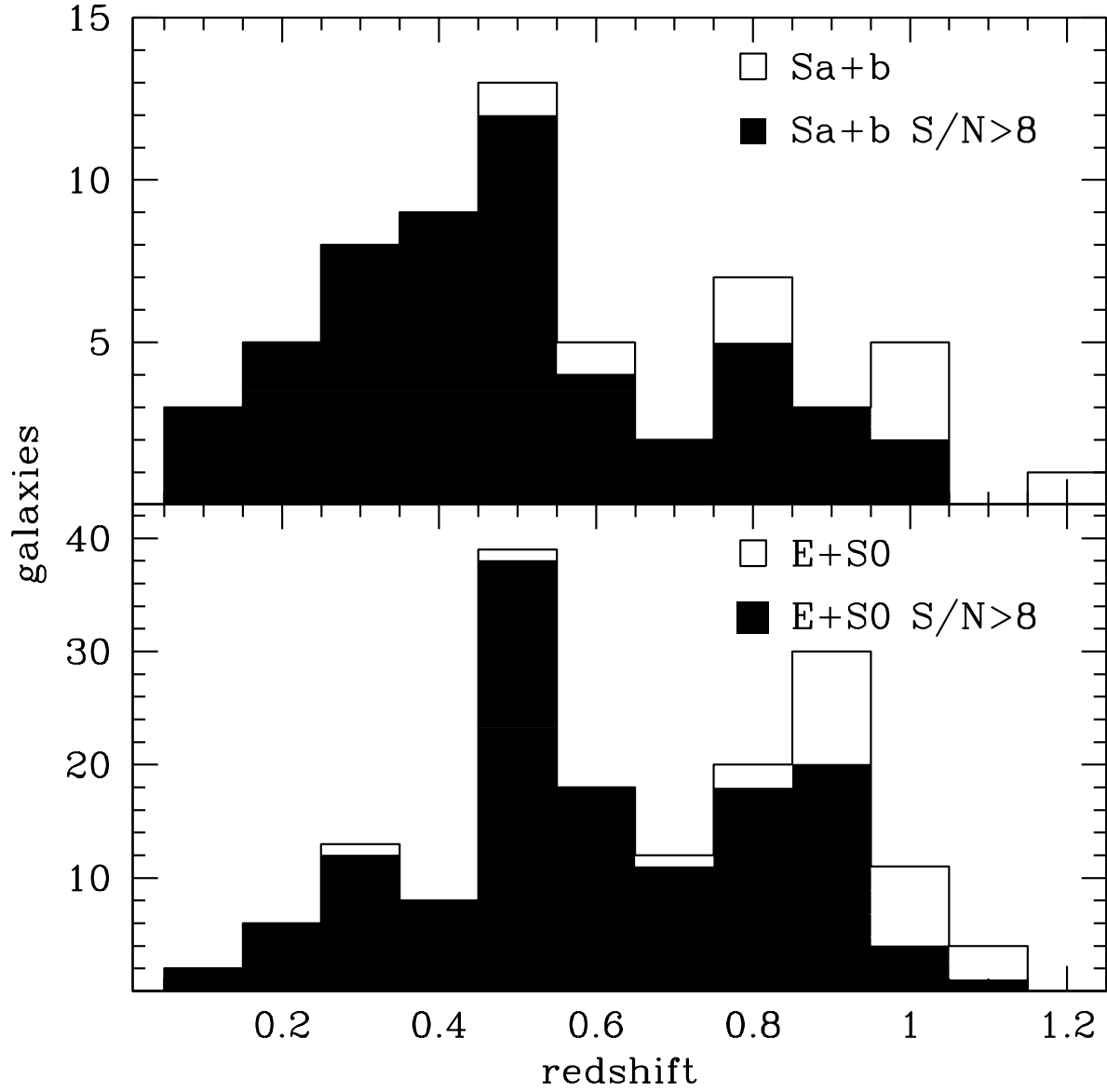


Fig. 8.— Redshift distribution of the early type spiral and E+S0 sample. Spectra with  $S/N > 8 \text{ \AA}^{-1}$  in the observers frame, for which velocity dispersions are typically available, are shown as a filled histogram.

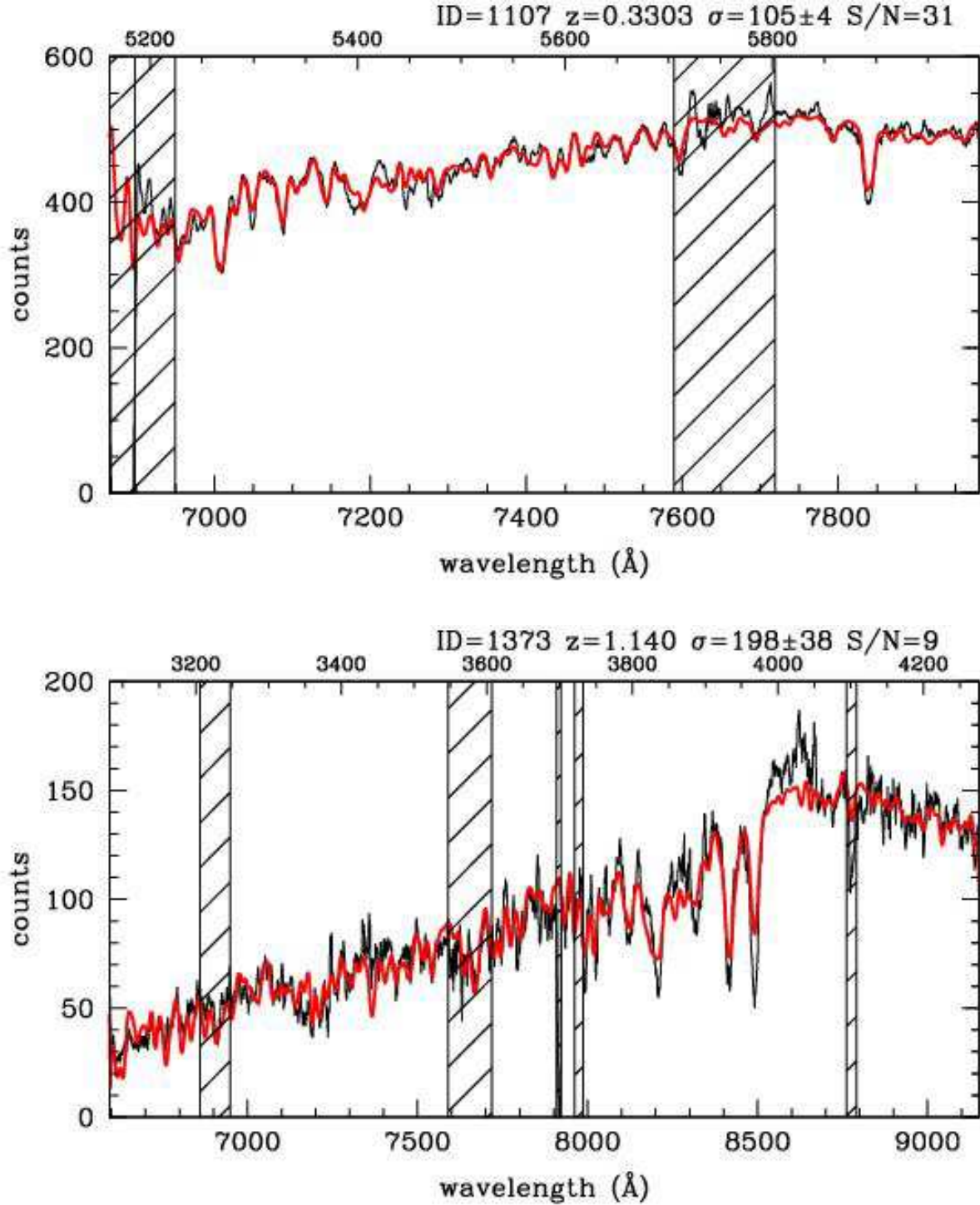


Fig. 9.— Example of an intermediate S/N spectrum (top) and the highest redshift spectrum with measured velocity dispersion (bottom). Both spectra are boxcar smoothed with a  $6\text{\AA}$  filter. The red line is the best fitting stellar template smeared at the best fitting velocity dispersion. Hatched regions represent those masked out during the fit. The top scale shows the rest frame wavelength and the derived quantities.

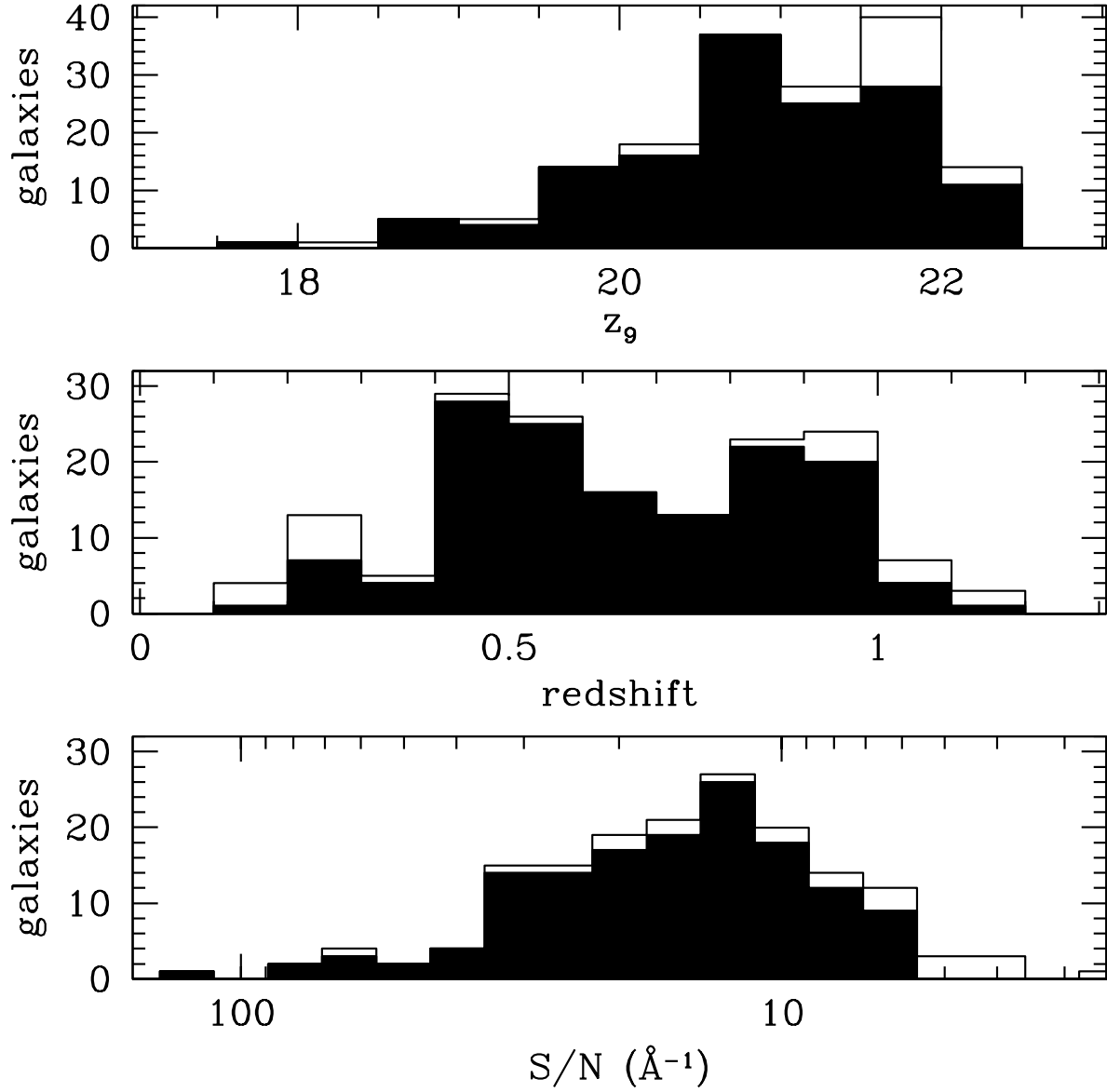


Fig. 10.— Success rate of velocity dispersion measurements. The upper panel shows the redshift distribution of early-type galaxies in the spectroscopic sample (empty histogram) and those with measured velocity dispersions (solid histogram). The middle panel shows the equivalent  $z_9$  luminosity distribution of the two samples. The lower panel shows the  $\langle S/N \rangle$  ( $\text{\AA}^{-1}$ ; observer frame) distribution of the two samples (note the inverted logarithmic x-axis).

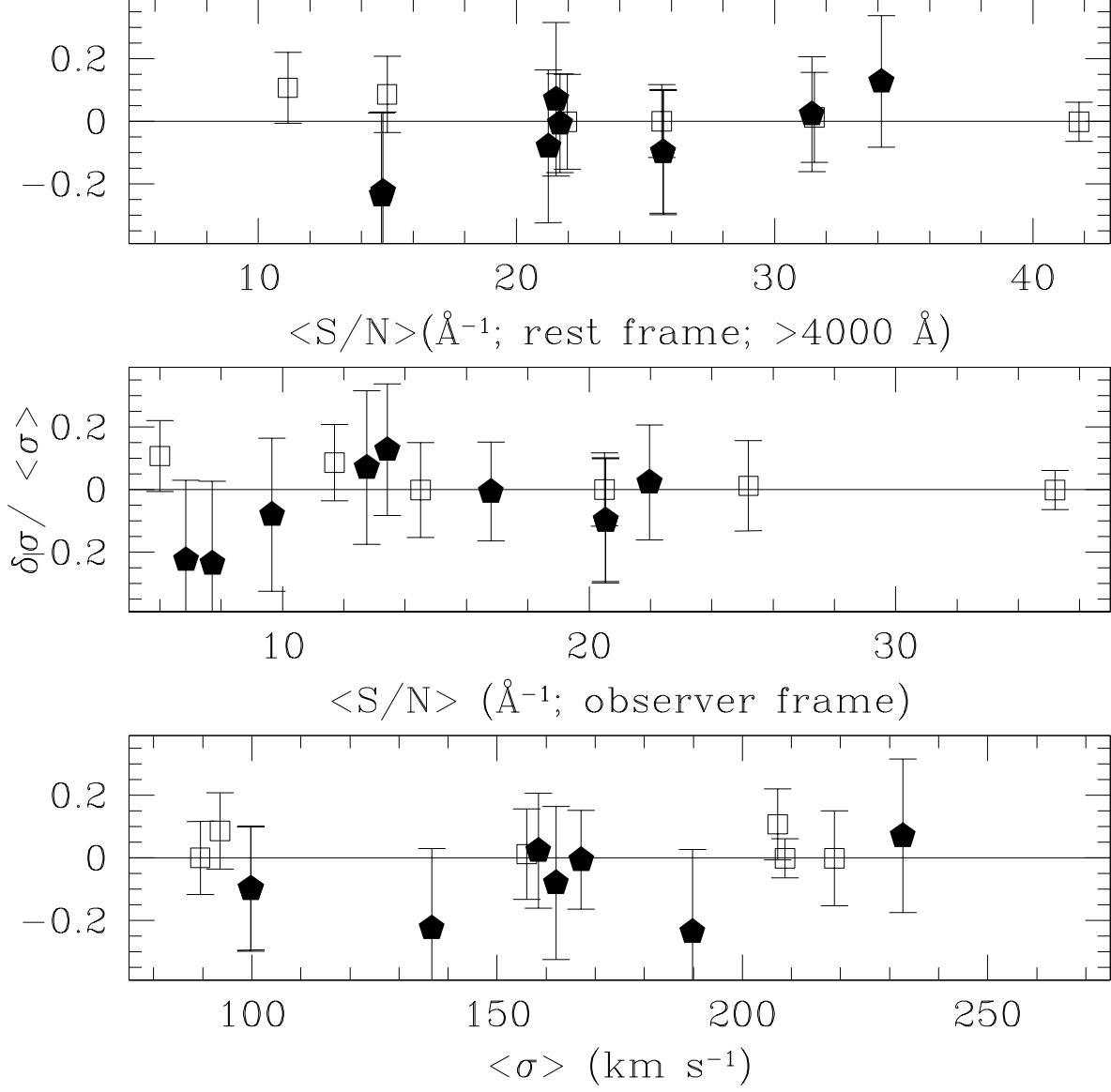


Fig. 11.— Velocity dispersion tests: I. Solid points represent comparisons with LRIS measurements from van Dokkum & Ellis (2003), open points represent internal DEIMOS comparisons for objects observed on different mask and slitlets configurations.

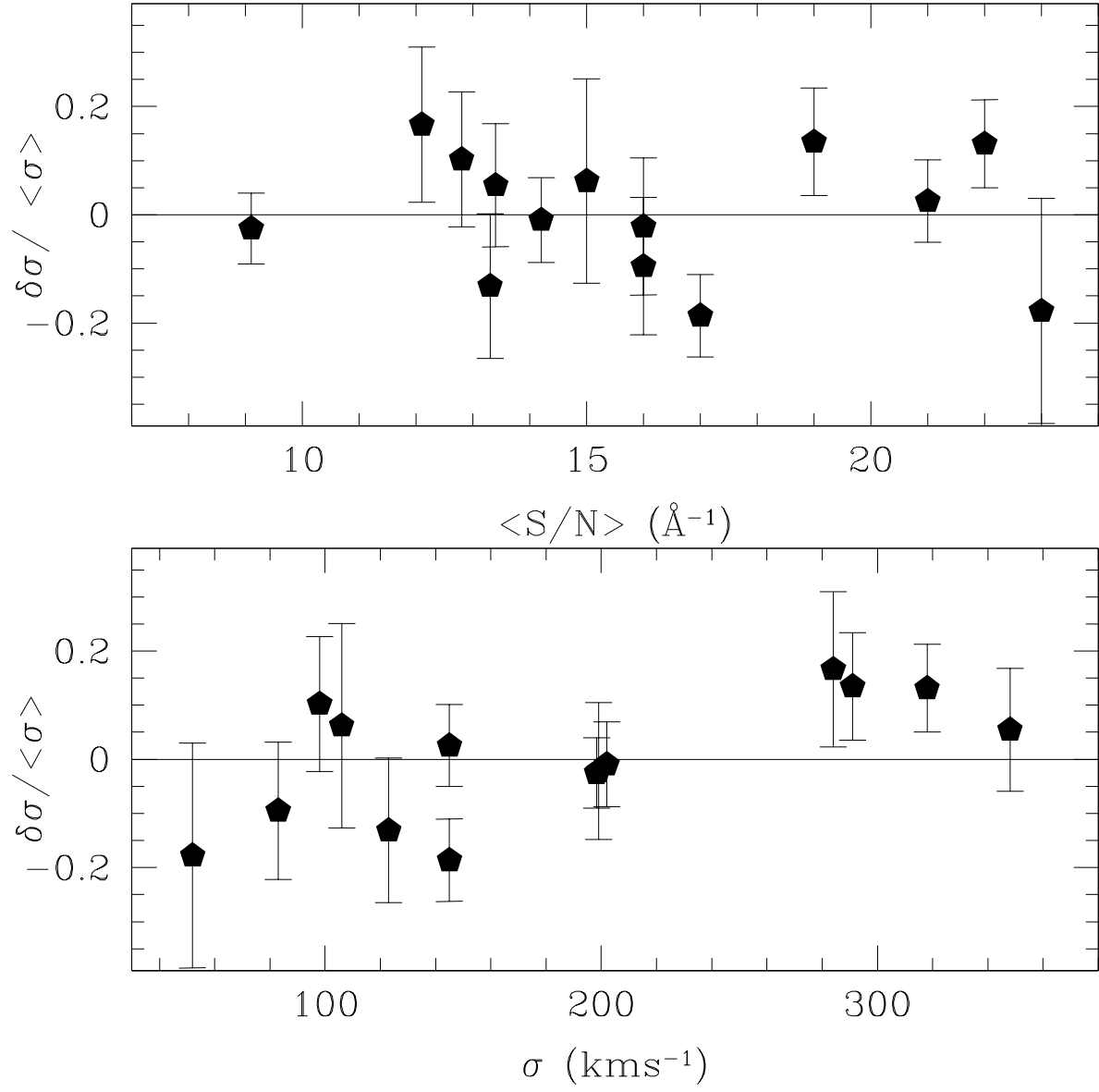


Fig. 12.— Tests on velocity dispersions II. Comparison between velocity dispersions obtained with two independent fitting methods (Treu et al. 2001a and van Dokkum & Franx 1996).

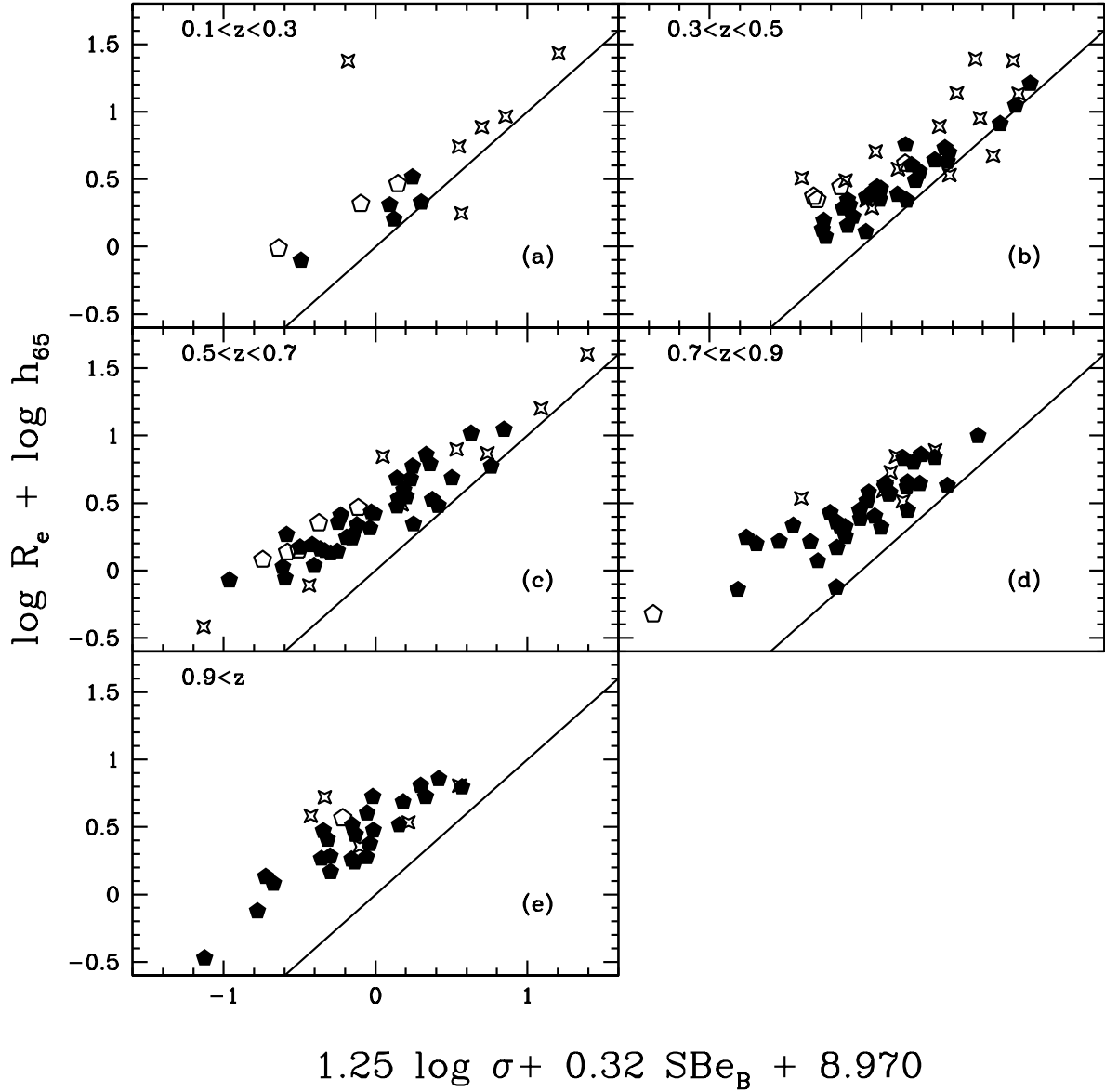


Fig. 13.— Location of survey galaxies in FP-space (the projection corresponds approximately to an-edge on view of the local FP) binned in redshift. Solid pentagons represent E+S0 galaxies with  $\sigma \geq 100 \text{ km s}^{-1}$ , open pentagons represent E+S0 galaxies with  $\sigma < 100 \text{ km s}^{-1}$ , while starred squares represent Sa+b galaxies. The local relationship is shown as a solid line.

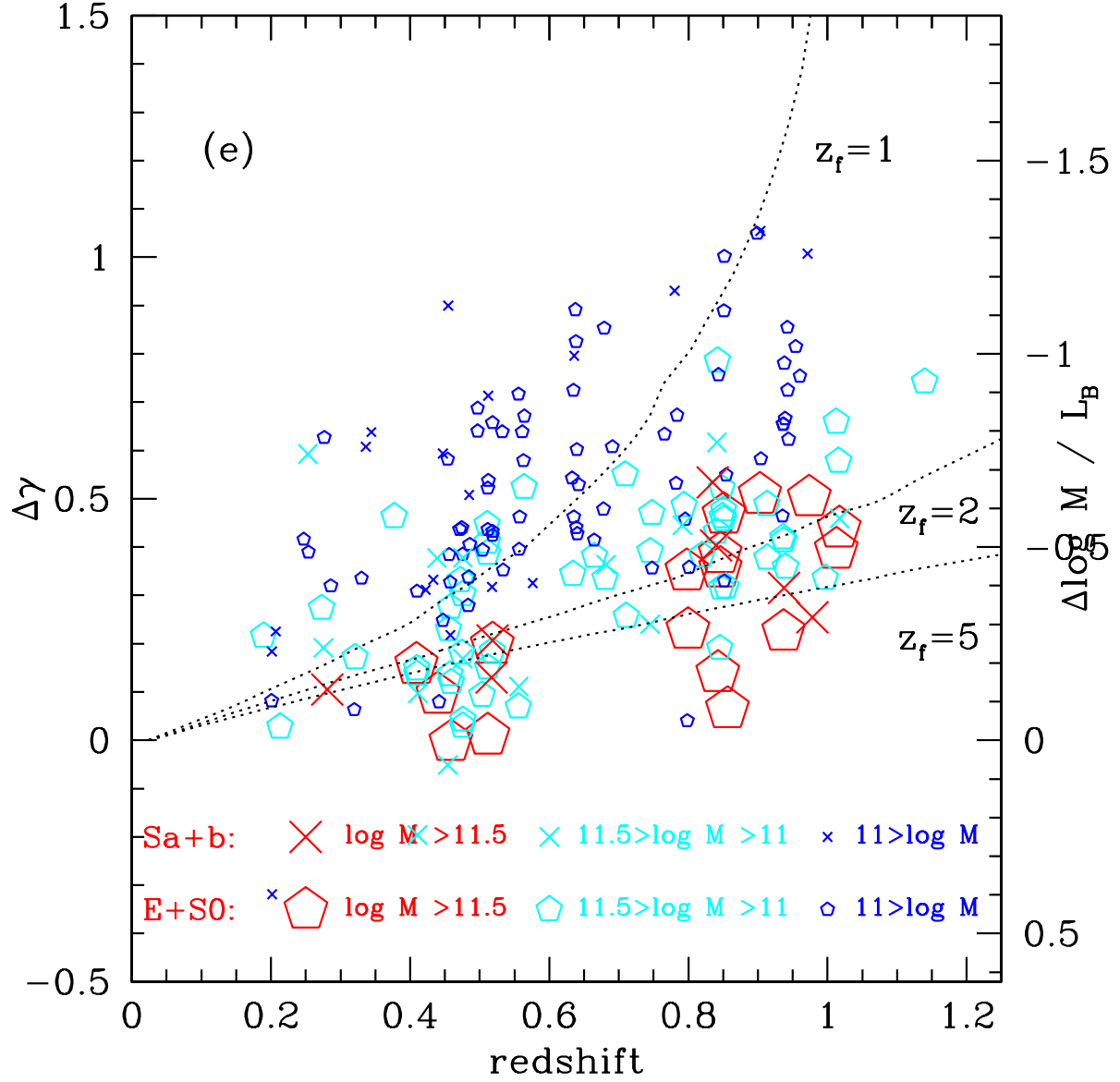


Fig. 14.— Offset from the local FP for the early-type and early-spiral galaxies, coded by mass (bigger symbols represent bigger dynamical masses). Notice that the offset from the local relationship and the scatter decrease with mass.



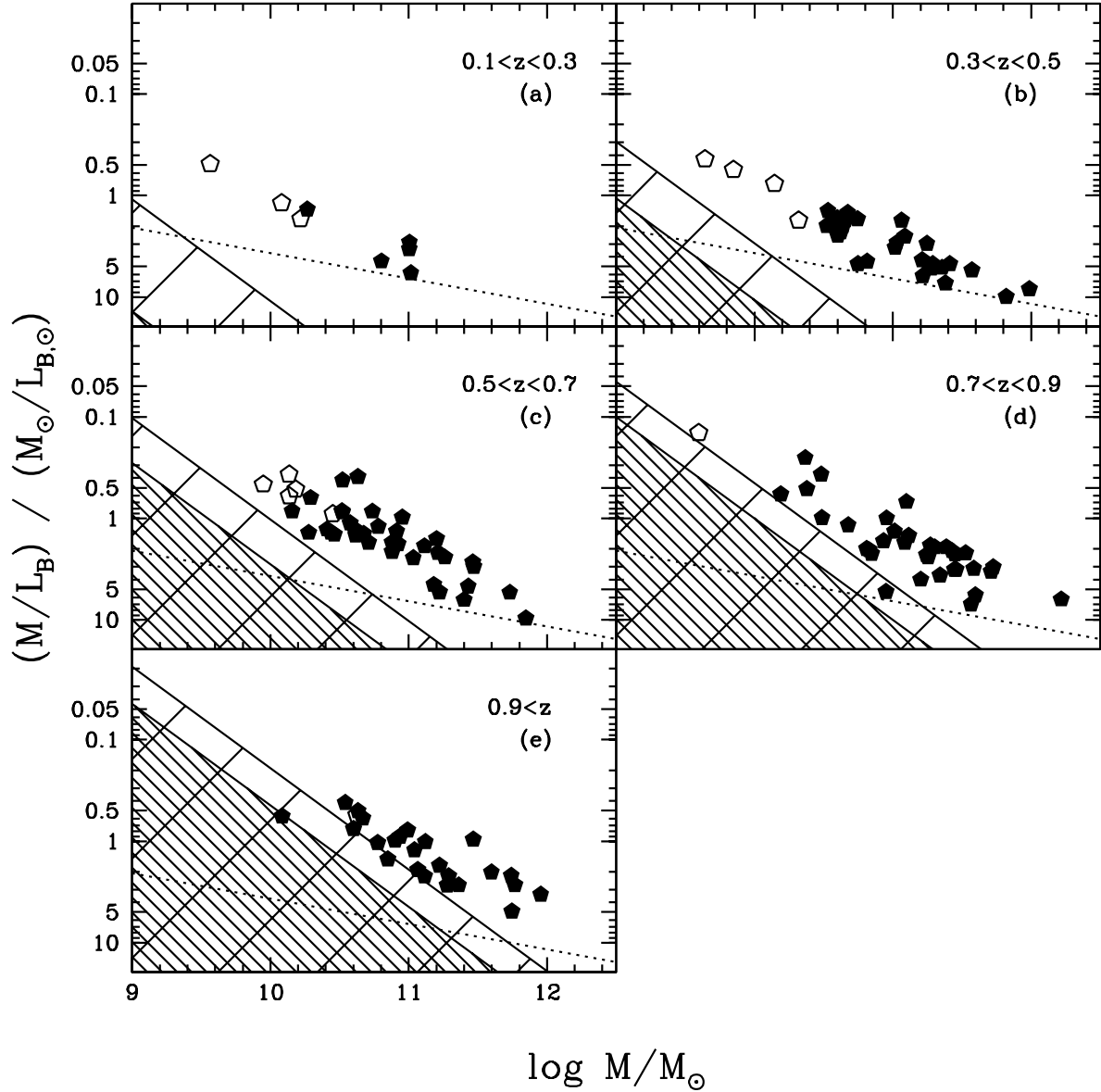


Fig. 15.— Effects of magnitude selection on the determination of the FP. The panels and symbols are as in Figure 13 but the FP is now projected on the M-M/L plane. The local relation is shown as a dotted line for comparison. Hatched regions are excluded by our  $z_9 < 22.43$  magnitude limit. The more densely hatched regions indicate the selection limit applicable for the lower end of the redshift bin, the more lightly hatched one to the upper end (assumed at  $z=1.1$  for panel e). The plots are for illustrative purposes only; the limits are approximate to a few hundreds of a magnitude because a fixed  $k$ -color correction was adopted and because the model photometry used to construct  $M/L_B$  is somewhat different from the SExtractor photometry in the selection process. The true selection criteria in the  $z_9$  band are faithfully implemented in our Montecarlo-Bayesian method.

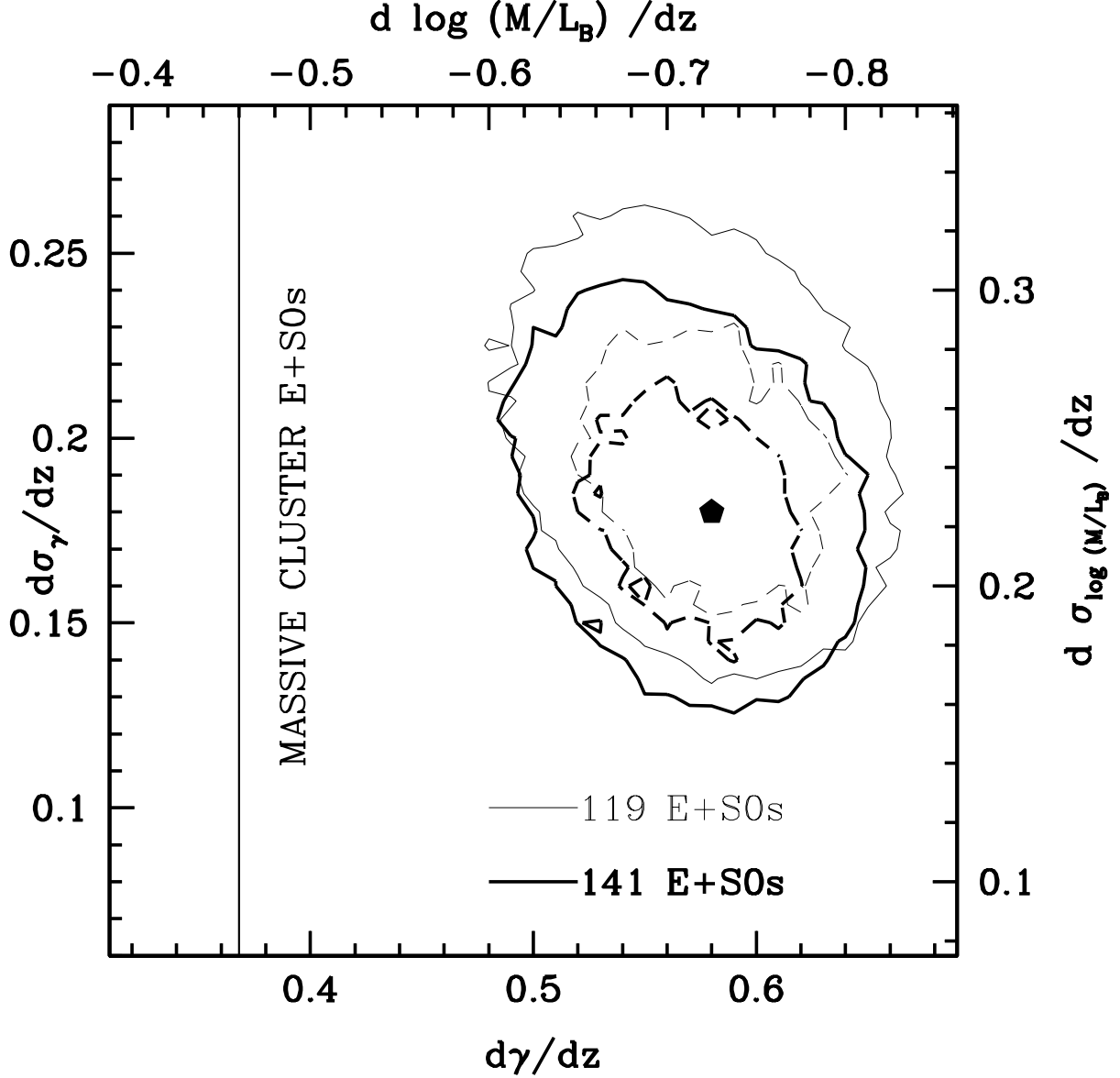


Fig. 16.— Probability contours for the evolution of the intercept  $d\gamma/dz$  and maximal evolution of the scatter  $d\sigma_\gamma/dz$  (dashed=68%; solid=95%). The maximum of the probability distribution is indicated by the solid pentagon. Thin contours represent the same probability levels for a smaller sample of 119 E+S0s, where 21 S0s have been excluded as possible early-spirals contaminants, see Section 2.2. The corresponding values in terms of  $M/L$  are shown on the top and right axis.

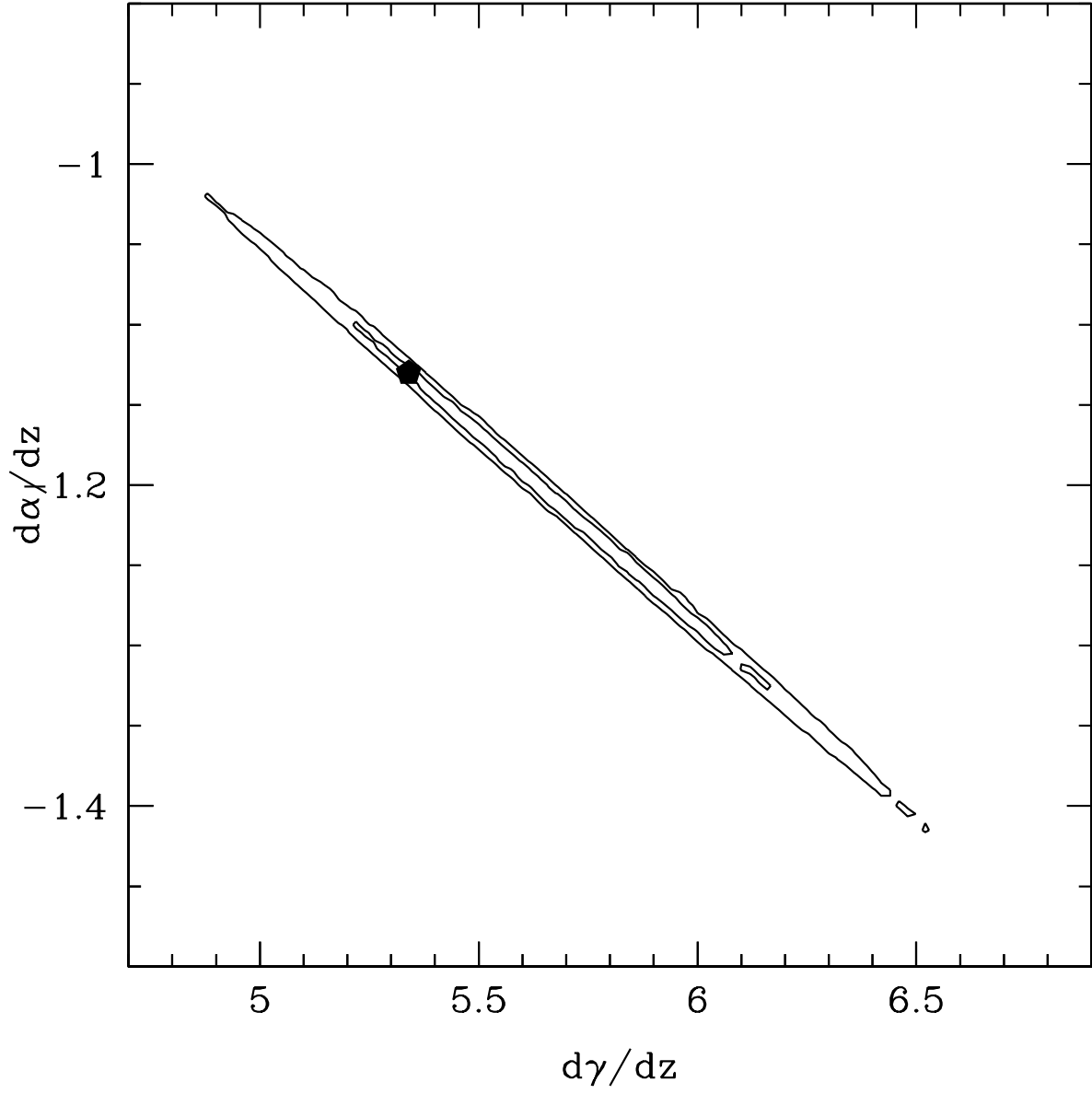


Fig. 17.— Mass-dependent evolution of the mass-to-light ratio: joint probability contours (68% and 95%) for evolution of the slope  $\alpha$  and the intercept  $\gamma$  of the FP, marginalized over the evolution of the scatter, and assuming  $\alpha(z) + 10\beta(z) + 2 = 0$ .

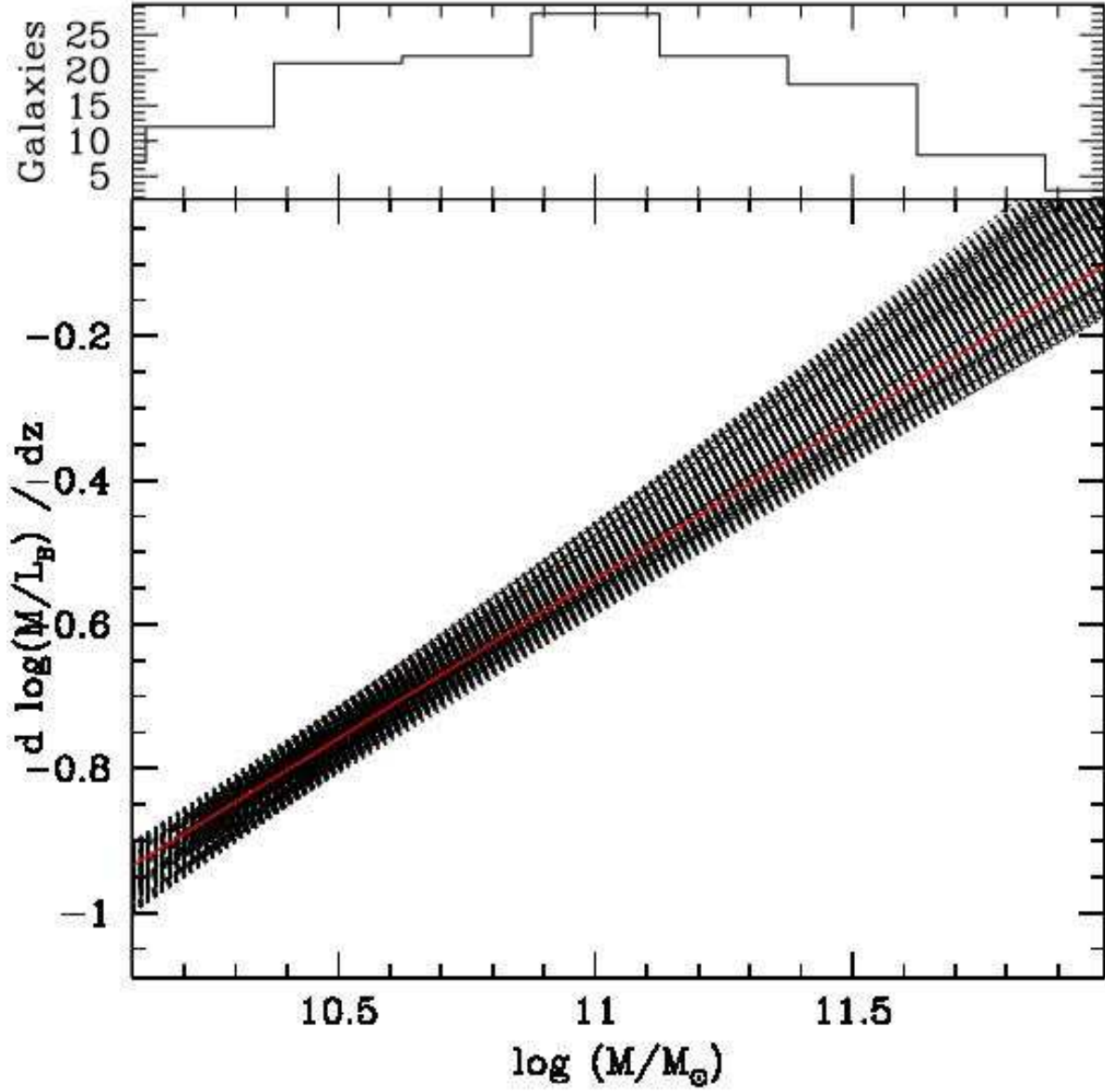


Fig. 18.— Bottom panel: the shaded area represents the 68% probability contour for the evolution of  $M/L$  as a function of  $M$ , obtained from Figure 17 with Equation 9. The solid red line corresponds to the best fitting model. Top panel: distribution of dynamical masses for our sample.

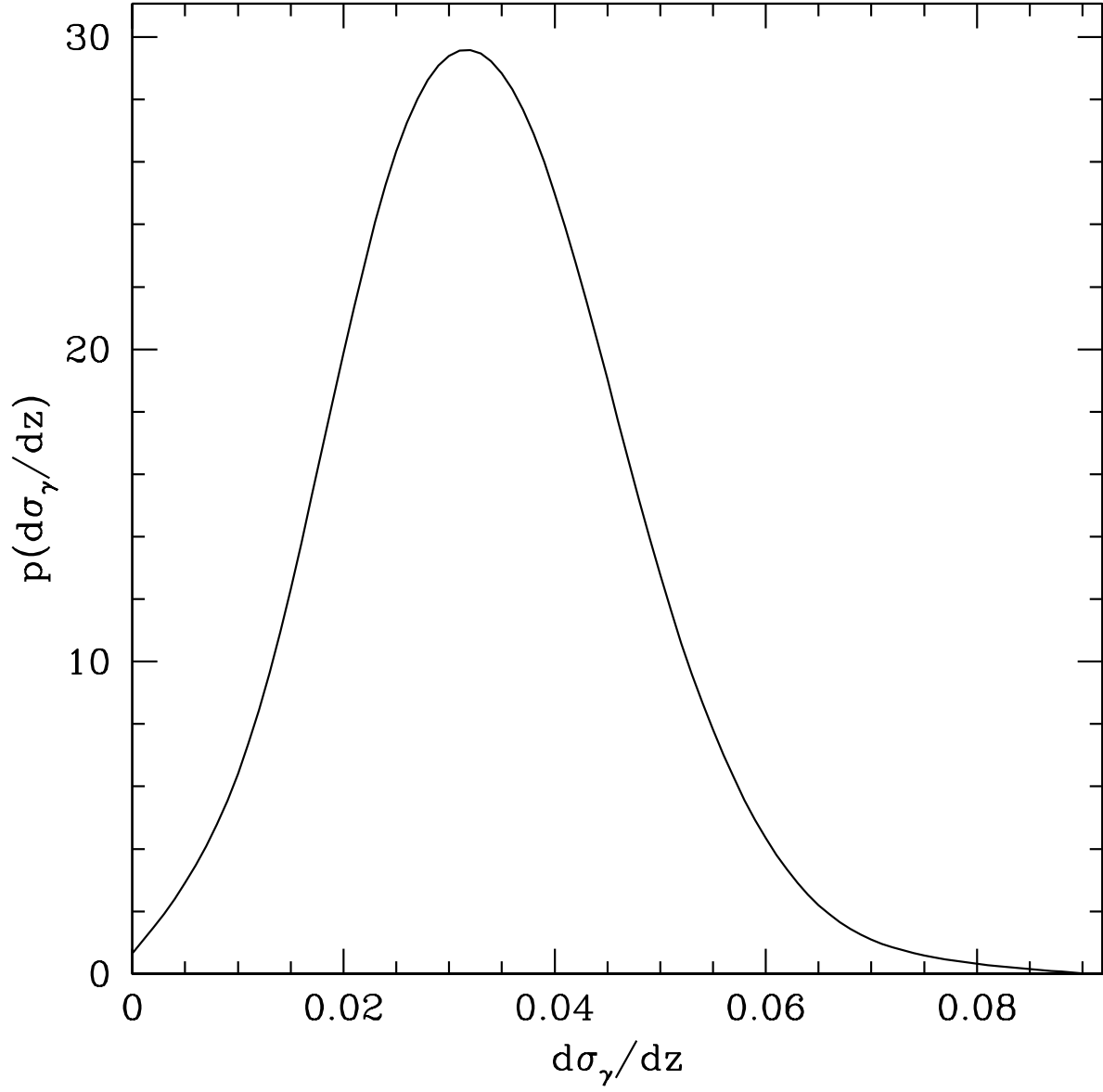


Fig. 19.— Probability distribution for the evolution of the scatter (in  $\log R_e$ ) of the FP, marginalized over changes in slopes and intercept. The scatter evolves as  $d\sigma_\gamma/dz = 0.032 \pm 0.012$  (68% limits).

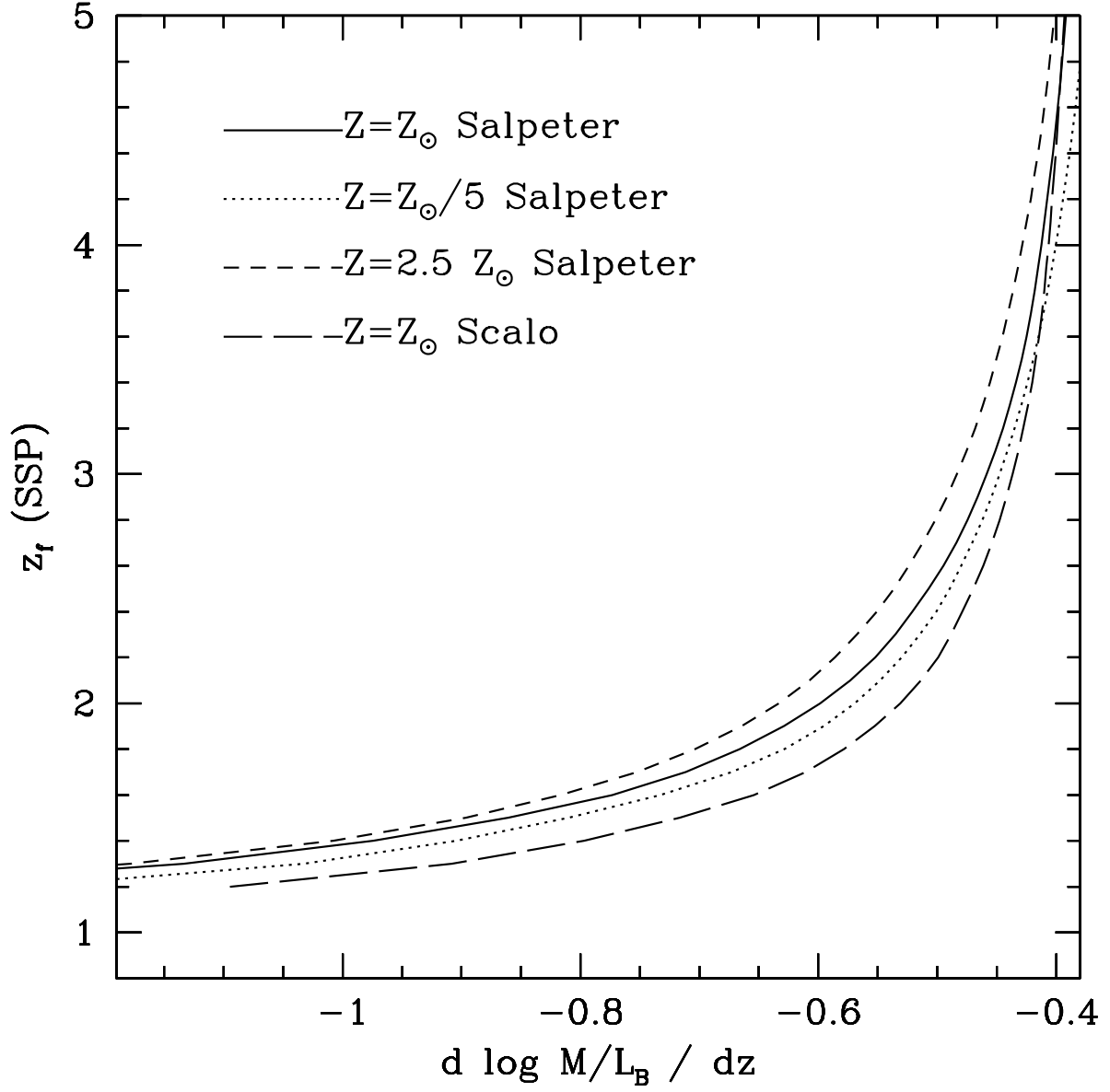


Fig. 20.— Redshift of formation as a function of evolution of the effective mass to light ratio for a set of simple stellar population models.

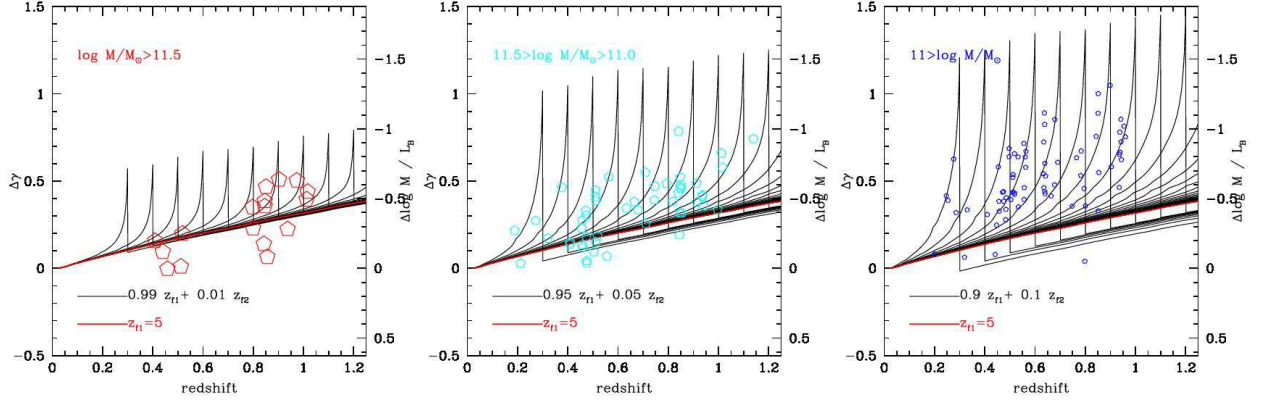
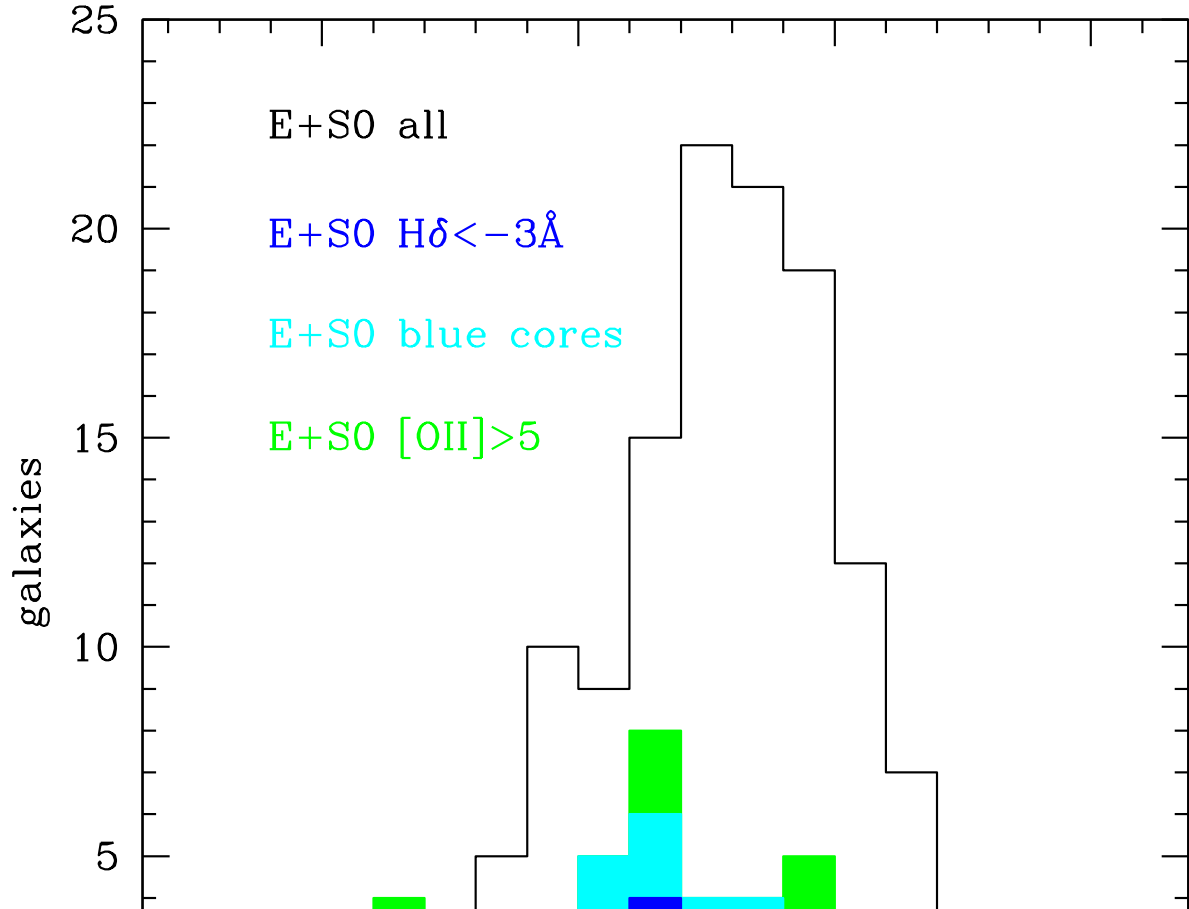


Fig. 21.— The solid black lines show the evolution of the mass-to-light ratio for a family of two-bursts models, where the majority of the stellar mass is formed at  $z_{f1} = 5$  and the rest (1-5-10% as indicated on the plots) is formed at  $z_{f2} < z_{f1}$  (secondary bursts are shown in steps of  $dz = 0.1$ , in the range  $z = 0.3 - 3$ ). For illustration the evolution of the mass-to-light ratio of the old component is also shown as a thick solid red line. The observed offset for our sample of E+S0 galaxies (coded by mass as in previous figures), is also shown for comparison. Note that this simple model covers the observed range of parameters, demonstrating that a simple two burst model is sufficient to reproduce the observations.



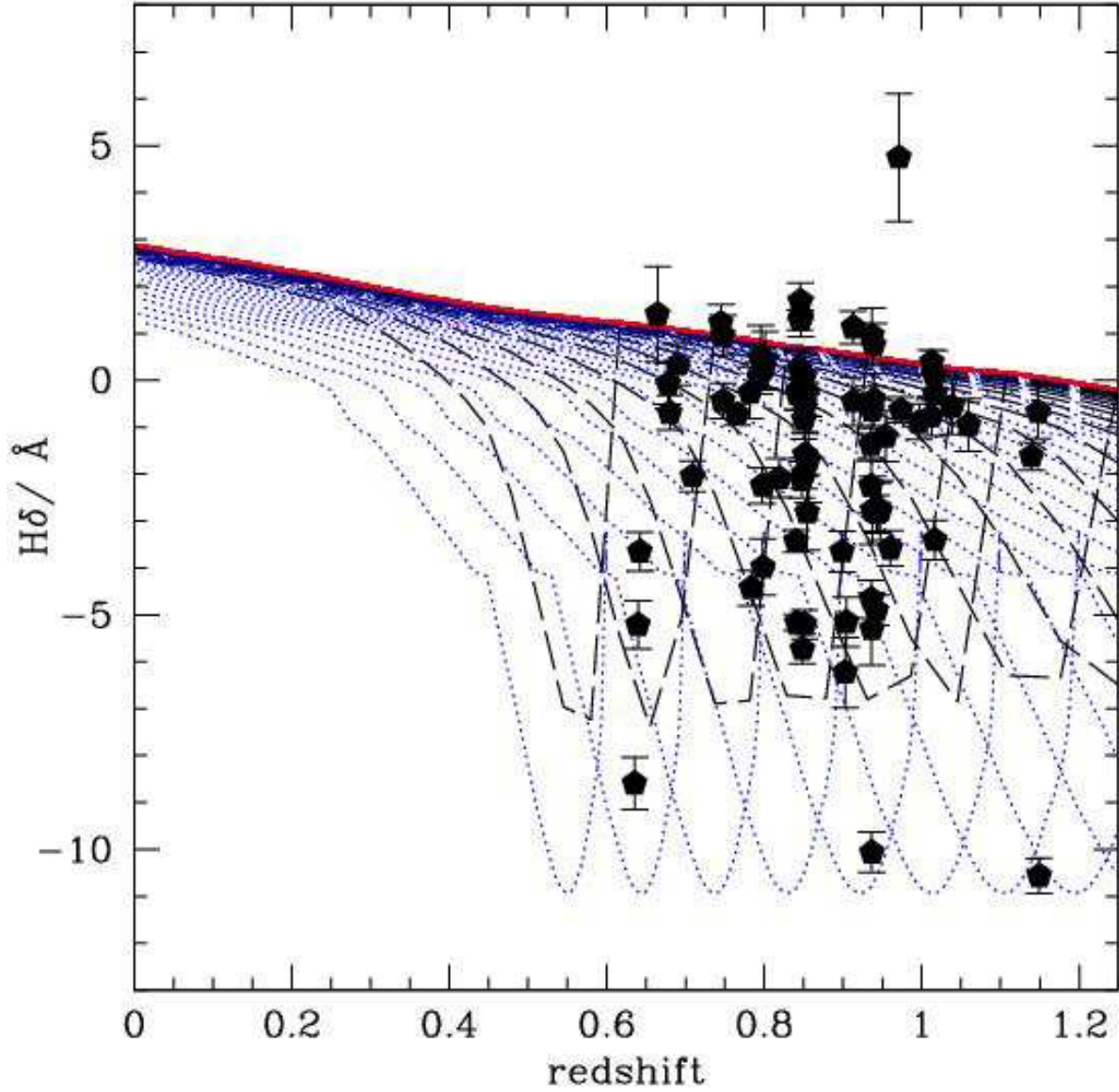


Fig. 23.—  $H\delta$  as a function of redshift for a family of two bursts models, consisting of a main burst forming 90% of the stellar mass at  $z_{f1} = 3$ , plus a secondary burst forming 10% of the stellar mass at  $z_{f2} < z_{f1}$  (lines as in Figure 21; models from Bruzual & Charlot 2003; solar metallicity). Measurements of  $H\delta$  for our sample of E+S0s galaxies are shown as filled pentagons.



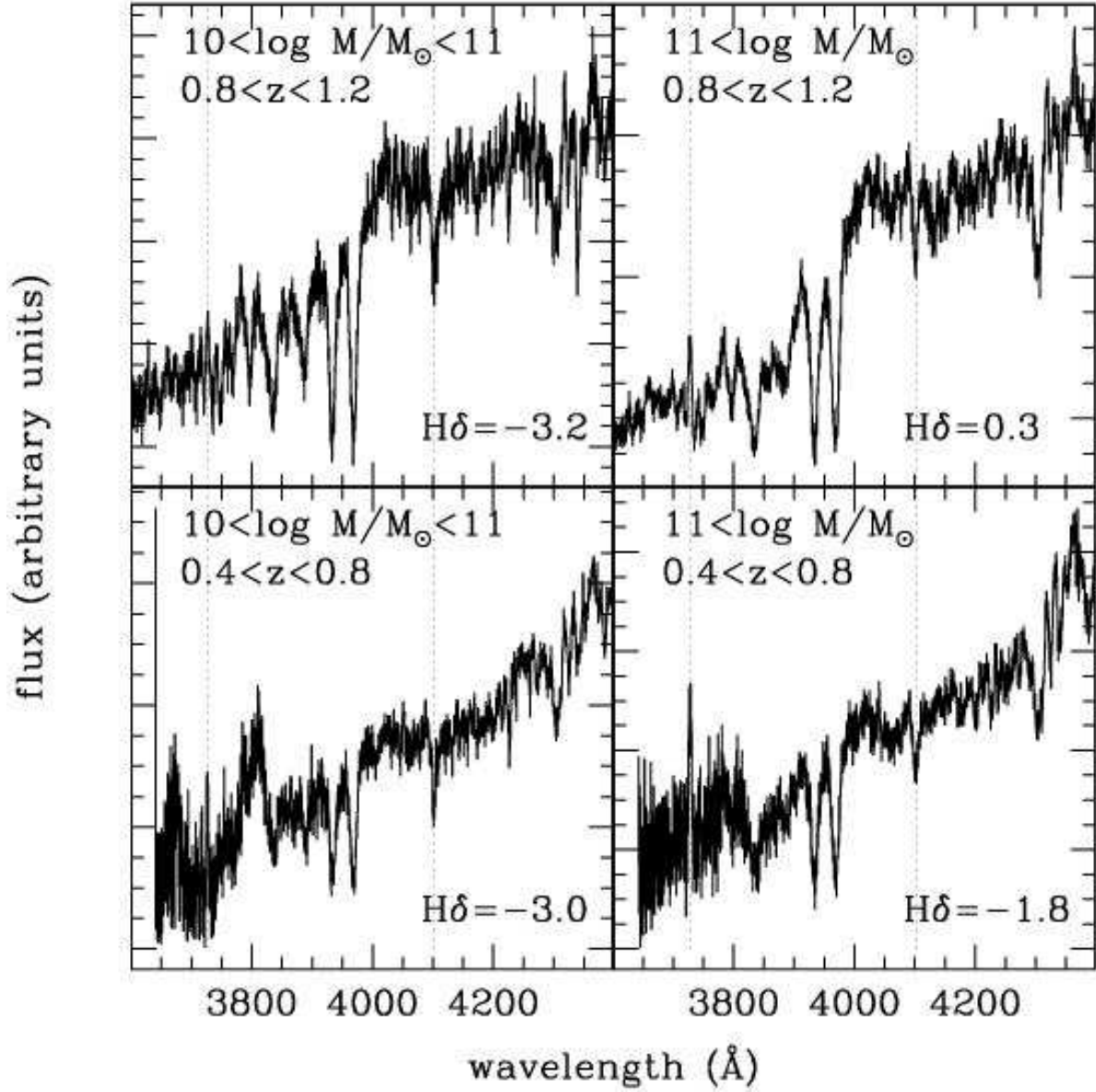


Fig. 24.— Co-added spectra of E+S0 galaxies, binned in mass and redshift. H $\delta$  in absorption is seen to be stronger for smaller mass systems, consistent with younger stellar ages than their massive counterparts.